

Aerosol Optical Depth over Oceans: High Space and Time Resolution Retrieval and Error Budget from Satellite Radiometry

Richard Wagener

Analytical Sciences Division, Brookhaven National Laboratory, Bldg. 490D, Upton, NY
11973-5000, USA

Seth Nemesure, and Stephen E. Schwartz

Environmental Chemistry Division, Brookhaven National Laboratory, Bldg. 426,
Upton, NY 11973-5000, USA

Received _____; accepted _____

Manuscript submitted to *Journal of Atmospheric and Oceanic Technology*.

1996 September 18

By acceptance of this article, the publisher and/or recipient acknowledges the U.S. Government's right to retain a nonexclusive, royalty-free license in and to any copyright covering this paper.

This research was performed under the auspices of the United States Department of Energy, under Contract No. DE-AC02-76CH00016.

Short title: AEROSOL OPTICAL DEPTH RETRIEVAL FROM SATELLITE

Abstract. A method to retrieve aerosol vertical optical depth at $0.64\ \mu\text{m}$ from satellite observations of cloud-free scenes over oceans with high spatial resolution ($\sim 1^\circ$) and instantaneous temporal resolution is described and evaluated. The observed radiance is treated as the linear sum of contributions to path radiance by different scattering processes in the atmosphere-ocean system. This treatment allows examination of errors in the retrieved vertical aerosol optical depth contributed by each process and approximation. Random error in retrieved aerosol optical depth is typically 0.03. The systematic error due to absolute calibration uncertainty in the measured radiance is 0.01. The largest errors and biases are due to radiative transfer approximations (+22%) and assumptions regarding aerosol microphysical and optical properties (-20%). The latter errors, which are due to the optical properties (*e.g.* phase function), vary systematically with latitude and season because of the variation of the mean observing geometry.

This method is applied to Advanced Very High Resolution Radiometer (AVHRR) Global Area Coverage (GAC) data, and example maps of aerosol optical depth are presented for specific dates in July and October 1986. The aerosol optical depth derived from the satellite data is suitable for examining large aerosol signatures by instantaneous comparison of the amplitude and location of aerosol plumes with model predictions based on meteorological conditions at and preceding the time of observation.

1. Introduction

Shortwave radiative forcing of climate due to an estimated global-average increase in anthropogenic sulfate aerosol optical depth of $\overline{\Delta\tau_a} = 0.04$ is of comparable magnitude, but opposite sign, to longwave forcing by greenhouse gases (Charlson *et al.* 1991; Charlson *et al.* 1992; Houghton *et al.* 1992; Houghton *et al.* 1994; Kiehl and Briegleb 1993; Boucher and Anderson 1995; Schwartz 1996). It is therefore important that this forcing be accurately represented in climate models. At present, this can be achieved only by evaluating the atmospheric aerosol loading and its geographical distribution by means of models that represent the processes governing the formation, transport and removal of these aerosols (Langner and Rodhe 1991; Taylor and Penner 1994; Benkovitz *et al.* 1994). However confidence in these models, and in turn in the modeled radiative forcing, is limited because of the limited data base of model evaluation through comparison of modeled aerosol loadings with observations. Most such comparisons are with *in-situ* measurements at the surface, mainly at land stations (Langner *et al.* 1993; Benkovitz *et al.* 1994). There is relatively little direct comparison over ocean locations and in vertical column. Satellite observations are needed to evaluate the performance of aerosol models over oceans and more generally to examine the magnitude and spatial and temporal variability of aerosol optical depth to infer natural and anthropogenic contributions. In principle, satellite observations are well suited to such comparisons (Penner *et al.* 1994; Hansen *et al.* 1993).

Aerosol loadings are highly variable in space and time, such that peak 24-hour average loadings are substantially greater than the means over longer time periods [*e.g.* Husain and Dutkiewicz (1990); see also Schwartz (1996)]. Benkovitz *et al.* (1994) reproduced this behavior in a recent study using a chemical transport model (Global Chemistry Model driven by Observational meteorological data, GChM-O). The vertical aerosol optical depth computed from the modeled sulfate loading over the North Atlantic

is typically $\tau_m < 0.03$ (assuming a mass scattering efficiency of $\alpha_{\text{SO}_4^{2-}} = 8 \text{ m}^2 (\text{g SO}_4^{2-})^{-1}$) (Charlson *et al.* 1992; Nemessure *et al.* 1995), but it can reach values in excess of 0.3 in large “episodes” in which compact parcels containing high aerosol concentrations are advected from industrial regions on the continents. This episodic nature of the aerosol loading computed by the GChM-O model contrasts strongly with that of models driven by monthly mean winds that consequently yield optical depths that are much more uniform spatially. The high temporal and spatial variability of aerosol loading suggests the necessity of characterizing aerosol optical depth from satellite data with spatial and temporal resolution comparable to that of variability exhibited in model calculations in order to evaluate model performance.

Previous studies of aerosol optical depths over oceans have employed Advanced Very High Resolution Radiometer Global Area Coverage (AVHRR GAC) data (Rao *et al.* 1989; Durkee *et al.* 1991; Ignatov *et al.* 1995). They have detected aerosols due to various regional sources, e.g. Saharan dust, smoke from large scale fires, and aerosols associated with industrialized areas. But the emphasis in these studies has been to produce wide spatial coverage by time averaging for periods of a week to a month, thereby masking the high spatial and temporal variability associated with the data and required for model evaluation.

The Rao *et al.* method has been employed in the production of weekly composite aerosol maps by NOAA since June 1987 (experimentally in its first two years, 1987-1989). The method determines aerosol optical depth from the observed normalized radiance through the use of a lookup table computed with a multiple scattering radiative transfer model for given (fixed) aerosol properties (size distribution, optical constants). NOAA also archives large events in daily “aerosol observation files”. The Durkee *et al.* algorithm, on the other hand, neglects multiple scattering, but allows for a variable aerosol scattering phase function dependent on the channel 1 ($\lambda = 0.64 \mu\text{m}$) to channel 2

($\lambda = 0.83 \mu\text{m}$) ratio.

Here we examine the systematic errors in the retrieved aerosol optical depth due to either of these approximations using a retrieval scheme based on the path radiance approximation (Gordon *et al.* 1988). In addition, we provide estimates of systematic and random errors due to the AVHRR calibration, digitization and noise characteristics, Rayleigh scattering, sunglint, sea foam, and ozone absorption. Since the inferred aerosol optical depth will be highly biased in the presence of even slight clouds, stringent criteria based on the color and the homogeneity of the neighborhood of each pixel are employed to reduce the likelihood of cloud contamination. The algorithm produces instantaneous optical depths averaged over individual GChM-O model grid cells ($1.125^\circ \times 1.125^\circ$) suitable for comparison with optical depths predicted by the chemistry model at the same locations and times (Berkowitz *et al.* 1994).

Although this paper focuses mainly on vertical aerosol optical depth and its errors, we also consider the directional scattering coefficient, *i.e.* that portion of the optical depth that contributes to scattering at the angle of observation; this quantity is directly derived from satellite radiance measurements and is thus independent of assumptions about aerosol microphysical properties.

2. Radiative transfer

The method described here applies only to cloud-free scenes of low optical depth over oceans (low surface albedo, and spatial uniformity). At the wavelength of the AVHRR channel 1, $\lambda = 0.64 \mu\text{m}$, the radiatively important processes contributing to the measured radiance are: ozone absorption (mainly stratospheric), scattering in the atmosphere (Rayleigh scattering on molecules and Mie scattering on particles, mainly in the troposphere, except after major volcanic events such as the 1991 eruption of Mount Pinatubo (Stowe *et al.* 1992)), and scattering processes at the surface (sunglint,

sky reflection, foam (white caps), and subsurface scattering). The scattering system is therefore treated as three distinct layers, as indicated in Table 1 and Figure 1. Table 1 also indicates the processes contributing to the radiance measured by the satellite radiometer and their radiative effects typical for mid-latitude summer, estimated using the radiative transfer approximation described below and data from Kaufman and Holben (1993). The relative contribution from Rayleigh and aerosol scattering, and sunglint varies strongly with viewing geometry (Kaufman and Holben 1993). Figure 1 shows the scattering geometry and defines the pertinent angles.

Table 1.
Figure 1.

The satellite observed normalized radiance is defined by $R(\theta, \theta_0, \phi) = \pi L / F_0$, where L is the satellite observed radiance and F_0 is the solar flux density or irradiance at the top of atmosphere. R is approximated by the sum of the radiance contributions of the several processes given in Table 1 as diminished by the transmittance of the overlaying layers (Gordon *et al.* 1988), where their water-leaving radiance has been decomposed into three separate components due to sunglint, sea foam, and subsurface scattering.

$$R = T_o(R_R + R_a + T_a T_R(R_s + R_f + R_{ss})) \quad (1)$$

Here T_o is the transmittance through (mainly) stratospheric ozone,

$$T_o = e^{-\tau_o(1/\mu + 1/\mu_0)}, \quad (2)$$

and the direct tropospheric transmittance

$$T_a T_R = e^{-(\tau_a + \tau_R)(1/\mu + 1/\mu_0)}, \quad (3)$$

where

τ_o = vertical ozone optical depth

τ_a = vertical aerosol optical depth

τ_R = vertical Rayleigh scattering optical depth

$$\mu = \cos(\theta); \theta = \text{viewing zenith angle}$$

$$\mu_0 = \cos(\theta_0); \theta_0 = \text{solar zenith angle}$$

$$\phi = \text{azimuth angle}$$

and the subscripts R , a , s , f , and ss refer to Rayleigh scattering of air (including sky reflection on the ocean surface), aerosol scattering, sunglint from the ocean surface, scattering by foam on the ocean surface, and ocean subsurface scattering, respectively. The aerosol contribution to the path radiance can be determined from the measured radiance R as

$$R_a = R/T_o - R_R - T_a T_R (R_s + R_f + R_{ss}) \quad (4)$$

provided the remaining quantities on the right hand side of Eq. 4 are known.

In principle, this equation should be iterated, because the right hand side contains a term T_a that depends on the aerosol optical depth to be determined from R_a . In practice, however, the satellite data are selected so that the ocean surface terms in parenthesis are small and a fixed aerosol optical depth of $\tau_a = 0.2$ can be assumed for the evaluation of T_a , without significant error (see Section 5.).

The approach to determine the quantities on the right hand side of Eq. 4 follows:

The normalized path radiance contribution due to Rayleigh scattering is given by

$$R_R = \tau_R \{p_R(\Theta_-) + [\rho(\theta) + \rho(\theta_0)]p_R(\Theta_+)\} / 4\mu, \quad (5)$$

where

$$\tau_R = \text{Rayleigh scattering optical depth}$$

$$p_R(\Theta) = \text{Rayleigh scattering phase function}$$

$$\Theta_{\pm} = \text{scattering angles [see Figure 1]}$$

$$\cos(\Theta_{\pm}) = \pm \cos(\theta_0) \cos(\theta) + \sin(\theta_0) \sin(\theta) \cos(\phi)$$

$$\rho = \text{Fresnel reflection function}$$

(Gordon *et al.* 1988). The first term $p_R(\Theta_-)$ is due to single scattering in the atmosphere. The second term represents photons that have been scattered once in the atmosphere and reflected once on the surface (“Sky reflection” R_{sky} in Figure 1).

The Rayleigh scattering optical depth for standard pressure at wavelength λ (μm) is given by

$$\tau_R = 0.008569\lambda^{-4} \cdot (1 + 0.0113\lambda^{-2} + 0.00013\lambda^{-4}) \quad (6)$$

(Hansen and Travis 1974).

The normalized radiance due to sunglint follows from Eq. 4.2-4 of Cox and Munk (1956):

$$R_s = \frac{\pi \rho(\gamma) P_s(\beta, W)}{4\mu \cos^4(\beta)} \quad (7)$$

where

γ = angle of incidence and reflection with respect to the wave slope normal

P_s = wave slope probability density function

β = wave inclination angle

W = surface wind speed, m s^{-1}

and following Cox and Munk (1956), the wave slope probability density function is given by a Gaussian distribution

$$P_s = (2\pi\sigma^2)^{-1} e^{-\tan^2(\beta)/2\sigma^2},$$

where

$$\cos(\beta) = (\mu + \mu_0)/(2\cos(\gamma))$$

$$\sigma^2 = (0.003 + 0.00512W)/2.$$

The normalized radiance due to scattering on foam at the ocean surface is given by

$$R_f = \mu_0 \cdot \begin{cases} 0 & \text{for } W \leq 4 \text{ m s}^{-1} \\ D_1 \rho_a C_D W^2 - D_2 & \text{for } 4 \text{ m s}^{-1} < W < 7 \text{ m s}^{-1} \\ (D_3 \rho_a C_D - D_4) W^2 & \text{for } W > 7 \text{ m s}^{-1} \end{cases} \quad (8)$$

where

$$\rho_a = 1.2 \text{ kg m}^{-3}, \text{ density of air}$$

$$C_D = \text{drag coefficient, m kg}^{-1} \text{ s}^2$$

$$D_{1,2,3,4} = \text{empirical coefficients}$$

given by Gregg and Carder (1990) as:

$$C_D = \begin{cases} (0.62 + 1.56W^{-1}) \times 10^{-3} & \text{for } W \leq 7 \text{ m s}^{-1} \\ (0.49 + 0.065W) \times 10^{-3} & \text{for } W > 7 \text{ m s}^{-1} \end{cases}$$

$$D_1 = 2.2 \cdot 10^{-5}$$

$$D_2 = 4.0 \cdot 10^{-4}$$

$$D_3 = 4.5 \cdot 10^{-5}$$

$$D_4 = 4.0 \cdot 10^{-5} \text{ m}^{-2} \text{ s}^2$$

approximating the empirical results of Koepke (1984).

Subsurface scattering on pigments in the surface layer of the ocean R_{ss} is dependent on the pigment concentration C_p and wavelength λ . For low pigment concentration in the ocean surface layer ($C_p < 1 \text{ mg m}^{-3}$), i.e. deep ocean, $R_{ss}(\lambda > 0.6 \mu\text{m}) < 0.0005$ (Hovis *et al.* 1980), which is about half of the digitization precision of the AVHRR (Sections 3. and 5.). Ignatov *et al.* (1995) determined that for deep ocean water (Morel and Prieur 1977, case 1 water) the reflectivity $\rho_{ss} = R_{ss}/\mu_0 = 0.0014 \pm 0.0006$ for the AVHRR channel 1 based on data summarized by Gordon and Morel (1983). Therefore, we set $R_{ss} = 0.0014\mu_0$ and limit our analysis to areas of low pigment concentrations as

indicated by climatological monthly averaged Coastal Zone Color Scanner (CZCS) data (Feldman *et al.* 1989).

The aerosol contribution to the normalized radiance is related to aerosol optical depth, analogously to Eq. 5 for Rayleigh scattering, as

$$R_a = \tau_a p'_a(\Theta_-, \Theta_+, \theta_0, \theta) \omega_0 / 4\mu \quad (9)$$

where

$$\begin{aligned} \tau_a &= \text{aerosol extinction optical depth} \\ \omega_0 &= \text{aerosol single scattering albedo,} \end{aligned}$$

and the combined phase function for aerosol scattering plus surface reflection

$$p'_a(\Theta_-, \Theta_+, \theta_0, \theta) = p_a(\Theta_-) + [\rho(\theta) + \rho(\theta_0)] \cdot p_a(\Theta_+)$$

with

$$\begin{aligned} p_a(\Theta) &= \text{aerosol scattering phase function,} \\ &\text{normalized such that } \int_{4\pi} p_a(\Theta) d\Omega = 4\pi. \end{aligned}$$

It may be observed that both the single scattering albedo and the phase function, $p_a(\Theta)$, are dependent on microphysical properties of the aerosol (refractive index and size distribution). In the absence of direct measurements of these properties assumptions are necessary to model single scattering albedo and phase function. In order to obtain a measure of the aerosol contribution to path radiance that is independent of assumptions of the microphysical properties of the aerosol we define and evaluate the quantity Ψ

$$\Psi = \omega_0 p'_a \tau_a = 4\mu R_a \quad (10)$$

which we denote the directional scattering coefficient. In the single scattering approximation this quantity is independent of the microphysical optical properties

of the aerosol, and it is therefore useful especially in distinguishing contributions to error in optical depth that are due to measurement errors from those that are due to uncertainties in aerosol microphysical properties. Given Ψ , Θ_- and independently determined or modeled ω_0 and p_a , the optical depth is evaluated as

$$\tau_a = \frac{\Psi}{\omega_0 p'_a}. \quad (11)$$

To evaluate τ_a we set $\omega_0 = 1$ and use an aerosol scattering phase function computed from Mie scattering calculations using a refractive index of $n_r = 1.5$ and a modified power law particle size distribution given by Rao *et al.* (1989):

$$\frac{dn}{dr} \propto \begin{cases} 0 & \text{for } r < 0.02 \text{ } \mu\text{m} \text{ and } r > 10 \text{ } \mu\text{m} \\ 1 & \text{for } 0.02 \text{ } \mu\text{m} < r < 0.1 \text{ } \mu\text{m} \\ r^{-4.5} & \text{for } 0.1 \text{ } \mu\text{m} < r < 10 \text{ } \mu\text{m} \end{cases}, \quad (12)$$

where n is particle number concentration, and r is particle radius. The sensitivity of optical depth on the assumed phase function and single scattering albedo is examined in Section 5..

3. Data processing

This section describes the computational method for the identification of cloud-free pixels and the determination of the aerosol optical depths from AVHRR GAC data. The GAC data consist of scanned satellite radiances in 5 channels with an instantaneous nadir field of view of $4 \text{ km} \times 1 \text{ km}$, sampled on a $4 \text{ km} \times 4 \text{ km}$ spacing. The spectral bandwidths of the two channels of data used here are given in Table 2.

Table 2.

Channel 1 and 2 data are provided in units of percent normalized radiance, digitized with 10 bit precision so that 1 count = 0.001069 normalized radiance. In the first processing steps the data are converted to fractional normalized radiance and normalized to the mean Earth-Sun distance, $d_0 = 1 \text{ AU}$, by $(1/100) \cdot (d/d_0)^2$, where d is the

Earth-Sun distance at the time of observation. Then they are recalibrated according to Rao *et al.* (1993) to compensate for the in-orbit sensitivity degradation of the detectors (Section 5.). For computational convenience the NOAA data files consisting of complete orbital scans are broken into “scenes” of approximately $2000 \text{ km} \times 2000 \text{ km}$.

The data are then subjected to the following series of tests in order to filter out cloud and sunglint contaminated pixels. These tests are designed to minimize the likelihood of contamination and consequently exclude some unknown fraction of “uncontaminated” pixels.

a. S_{12} Threshold

The channel 1 to channel 2 radiance ratio, S_{12} , is computed. Based on the observations that $S_{12} \sim 1$ for totally overcast pixels and pixels contaminated by sunglint, and that $S_{12} > 1.5$ for cloud-free pixels in the anti-sunward direction, pixels with $S_{12} < 1.5$ are removed. Likewise the criterion $S_{12} < 1.5$ automatically filters out data over land surfaces since S_{12} is invariably less than 1 over land. For a small fraction of the pixels ($N/N_{tot} < 0.02\%$) $S_{12} > 3.5$ (Figure 2). This is probably caused by the slight spatial offset between the channel 1 and channel 2 field of views, which makes it possible for one channel to include the edge of a cloud whereas the other channel does not. These pixels are therefore eliminated as well.

Figure 2.

b. Spatial Uniformity

This test for cloud-contaminated pixels examines the spatial uniformity of neighboring pixels. If the channel 2 normalized radiance of any of the four nearest neighbors differs by more than 0.0053 (5 digital counts) from the center pixel, then the pixel is classified as partly cloudy and rejected.

c. Distancing

Pixels immediately adjacent to cloudy pixels can be contaminated but escape detection in the first two screening tests above. To further distance the remaining pixels from the pixels identified so far as cloud or sunglint contaminated, the four pixels directly adjacent to a previously rejected pixel are rejected as well.

d. High Sunglint

In addition to the pixels removed by the S_{12} *Threshold* test, pixels with normalized sunglint radiance R_s calculated from Eq. 7 exceeding $5 \cdot 10^{-5}$ are removed in this last step. The surface wind speed necessary for the calculation of R_s is obtained from archival data of the 6 h forecast model of the European Centre for Medium-Range Weather Forecasts, Research Department (1988, ECMWF). The surface winds from the most recent model time step are used ($\Delta t < 6$ h). The very conservative cutoff is chosen, because the Cox and Munk formulation apparently underestimates the true sunglint (Figure 3), and because the representativeness of the 6 h ECMWF forecast winds for the sea surface conditions at the time of the satellite observation is questionable.

Figure 3.

For the pixels that pass all the above tests, Ψ and τ_a are calculated according to Eqs. 10 and 11, using Eq. 4 with $R_{ss} = 0$. The time tagged Ψ and τ_a from each satellite overpass are mapped onto the GChM-O grid ($1.125^\circ \times 1.125^\circ$) and aggregated, keeping track of the mean values and two quality indicators: the number of AVHRR pixels included in each GChM-O grid cell average, and the corresponding standard deviation of τ_a . The scattering angle Θ_- is also averaged for each grid cell in order to facilitate calculation of aerosol optical depth from the directional scattering coefficient Ψ for different models of the microphysical optical properties of the aerosol. There are few instances at high latitudes where cloud and glint free areas overlap in successive satellite overpasses (3% of all grid cells). Therefore, except for those cases, each grid

cell contains data only from a given time period, spanning at most 1 minute. Since the time of observation is stored in the GChM-O grid as well, it is possible to interpolate the GChM-O model predictions (saved every 6 h) or the ECMWF meteorological data to the actual time of observation before the comparisons are performed (Berkowitz *et al.* 1994).

4. Results

To evaluate the procedures in Section 3., we applied them to NOAA 9 AVHRR GAC data for 1986 July 27 and October 15. The July data are from 10 successive orbits and the October data include all 14 orbits spaced approximately 100 minutes apart. Sample scan lines, east of the U.S. coastline (position of the pixel in the middle of the scan line: latitude 30° , longitude -54°) are shown in Figure 4 for July 27 and Figure 5 for October 15. Also shown are the calculated contributions from Rayleigh scattering (including sky radiance; Eq. 5) and sunglint (Eq. 7). The satellite observed normalized radiance R (Eq. 1) has been converted to an effective “top of troposphere” normalized radiance by dividing by the transmission of the ozone layer T_o computed from the daily gridded Total Ozone Mapping Spectrometer (TOMS) total ozone column data (Guimaraes and McPeters 1990) and the ozone absorption cross-section (Inn and Tanaka 1953) averaged over the AVHRR channel 1 transmission, $\sigma_o(\text{Channel } 1) = 2.90 \cdot 10^{-25} \text{ m}^2$.

The scan direction, increasing pixel position, is from east to west and covers roughly 2000 km. The nadir is at pixel position 192. Since NOAA 9 is in an afternoon orbit ($\sim 14:30$ local time of ascending node) the sunglint region is confined to the western part of the scan lines. At this latitude (30° N) the normalized sunglint radiance is much higher in July than in October. The Rayleigh scattering contribution is lowest near nadir (center of scan line) and increases toward higher viewing zenith angles.

Figure 4.

Notice the expanded scale on the ordinate of Panels 4d and 5d. Most of the

Figure 5.

“uncontaminated” pixels differ by only a few digital counts from $R_R + R_f$. Because it is this difference between the observed radiance and that due to $R_R + R_f$ (Panels 4d and 5d) that is converted *via* Eq. 11 to aerosol optical depth, the resulting optical depth (Panels 4e and 5e) is subject to significant digitization noise (1 count corresponds to $\tau_a = 0.02$ near nadir [pixel position 192] decreasing to $\tau_a < 0.01$ at $\theta > 35^\circ$ [pixel position < 80]).

To give an indication of the relative importance of each screening test described in Section 3., Table 3 lists the percentages of pixels removed in each step. The percentages are evaluated on each of $\sim 2000 \text{ km} \times 2000 \text{ km}$ regions and the ranges indicated in Table 3 denote the observed variations of the percentages over the 70 such regions for July 27. Of the total number of $1.125^\circ \times 1.125^\circ$ grid cells covered by the AVHRR overpass, 16% contain an optical depth value. For those optical depth values on average 15% of the available pixels were used. The median number of clear pixels in grid cells that contain at least one clear pixel is 50. Therefore, the averages and standard deviations are statistically meaningful.

Table 3.

a. Retrieved optical depth

The optical depths determined by Eq. 11 on the two days analyzed above (1986 July 27, and October 15) are shown in Figure 6. Note that the land areas are entirely eliminated by the S_{12} criterion, although some inland lakes are represented. Note also the banding of the regions for which data are obtained at mid and low latitudes. This is due to the orbital motion of the spacecraft and the rejection of more than half of each scan swath due to sunglint (Figures 4 and 5). The data at high latitudes have been eliminated with a cutoff on the cosine of the solar zenith angle because the linear approximation employed does not apply at high slant path ($\mu_0 < 0.3$, Figure 7).

Figure 6.

Other obvious features in Figure 6 are the enhanced aerosol signatures in the trade

Figure 7.

wind regions due to mineral aerosols from deserts (e.g. Sahara) and the low optical depths values in regions of the South Atlantic removed from continental influences. There are some areas of enhanced aerosol optical depth in the vicinity of Central America, East Asia, and Northern Europe that could be due in part to anthropogenic aerosols.

b. Sampling Issues

To interpret the retrieved aerosol optical depth one must pay attention to possible biases due to sampling constraints imposed by the satellite observing geometry and the computational algorithm (Section 3.). The subsatellite track and the sunglint avoidance zone restrict aerosol retrievals to the afternoon (14:00 to 16:00 local time) and therefore catches only one phase of any diurnal cycle.

The cloud screening steps also eliminate areas associated with clouds that might have enhanced aerosol optical depth, due possibly to the influence of relative humidity (Nemesure *et al.* 1995), resulting in a negative bias. The S_{12} ratio test in addition to screening sunglint and clouds might also eliminate a portion of high optical depth and large particle aerosol (*e.g.* mineral aerosol in the tropical Atlantic).

The scattering angles fall in the range between 100° and 180° . The median scattering angle is a function of latitude and because of uncertainties in the phase function could introduce an artificial latitudinal variation in aerosol optical depth (Section 5.).

c. Statistics

The standard deviation of the aerosol optical depth averaged over the 1.125° grid cells, is shown in in Figure 8 for 1986 July 27 as a function of the grid cell average τ . The standard deviation is composed of a contribution from digitization and detector

sensitivity noise, which are independent of the average optical depth in each grid cell, and a contribution, which increases with optical depth, due to the intrinsic variation of optical depth over the grid cell. The digitization noise is 0.5 counts or $\Delta_d R = 0.00053$. The AVHRR radiometers were designed to achieve a noise level of $\Delta_n R = 0.0017$, which, according to (Rao 1987), has been attained or exceeded in all the radiometers. Thus the combined random error of individual normalized radiance measurements is $\Delta_r R \leq 0.0018$, which corresponds to an error in optical depth of $\Delta_r \tau_a \leq 0.024$ (median over observing geometries). The observed median standard deviation for July 27, $s(\tau_a) = 0.014$ (Figure 8), is consistent with these instrument characteristics and is taken to be representative of the random errors of individual optical depth retrievals. Because the 1.125° grid cells average tens to hundreds of points, these instrumental random errors decrease by a factor of $N^{1/2}$ in the grid cell average and can therefore be neglected.

Figure 8.

We examined the median standard deviation, $s(\tau_a)$, for any systematic dependencies on μ_0 , μ , ϕ , and Θ_- . The only significant dependencies are the approximate proportionality between $s(\tau_a)$ and μ and $1/p_a(\Theta_-)$. These are expected, because, for a constant optical depth, the signal (normalized radiance R_a) increases as $1/\mu$ and $p_a(\Theta_-)$.

d. Latitudinal distribution

For a preliminary examination of the potential for detecting latitudinal variations in differences in aerosol optical depth due to varying aerosol column burdens, Figure 9 shows the optical depth as a function of latitude. For each of the two dates the high values in the tropics are probably associated with mineral and biomass-burning aerosols. As these aerosols are concentrated in the subtropical Atlantic, this peak is exhibited more prominently in the July data, longitude range 100°W to 150°E , than in the

October data, which have global coverage.

Figure 9.

The locally weighted scatterplot smoothing (Cleveland 1979, LOWESS) curves in Figure 9 follow the local median values and are therefore representative of the background aerosol optical depths. The variation of this background optical depth with latitude could be due in part to error in the assumed aerosol phase function (Section 5.).

The high values at the northern limit of the July data are concentrated in the Barents Sea, northeast of the Scandinavian peninsula, and may be indicative of anthropogenic aerosol. The high values near 45°N in the October data are concentrated in the Northern Pacific and are probably of Asian origin.

e. Reproducibility

The Barents Sea data for 1986 July 27 are particularly valuable because they lie in an area of overlapping orbits and they happen to include regions exhibiting relatively high values of $\tau_a \sim 0.5$. In the latitude range 66° – 72° the observed optical depths varied substantially and systematically as a function of longitude (Figure 10). Notably, the data from five consecutive orbits show the same trend without obvious systematic residual dependence on solar or viewing zenith angles.

Figure 10.

5. Error analysis

a. AVHRR detector noise and calibration uncertainty

In Section 4. we estimated the grid cell average error due to digitization and detector noise as $\Delta_r \tau_a \sim 0.014N^{-1/2}$, where N is the number of pixels per grid cell with median value $N = 50$ (Figure 8). Here we estimate the systematic errors that are due to the absolute calibration uncertainty of the AVHRR channel 1 detector.

The recent in-flight calibration of the AVHRR shortwave channels using relatively stable areas of known surface albedo (Rao *et al.* 1993) has resulted in a sensitivity

degradation correction that increases the channel 1 and 2 radiance for October 1986 by 8% to 10% compared to the pre-flight calibration. The corresponding change in retrieved optical depth is illustrated in Figure 11. The new calibration results in a systematic increase in optical depth of 0.02 with an estimated uncertainty of $\Delta_c \tau_a = 0.01$ changing to a relative error for $\tau_a > 0.2$ of $\frac{\Delta_c \tau_a}{\tau_a} = 5\%$ based on the quoted calibration uncertainty of 5% (Rao *et al.* 1993). All the results presented here have been evaluated using the new calibration.

Figure 11.

b. Ozone transmission

As the ozone transmission term, T_o , is a correction term to the observed radiance, R (Eq. 4), its effect is like a calibration correction, and therefore any uncertainty in the ozone optical depth results in a linear offset in retrieved aerosol optical depth. The ozone optical depth for the observed geographic areas on October 15 has a mean of $\tau_o = 0.021$ and standard deviation $\sigma_{\tau_o} = 0.002$. Even with a very conservative uncertainty estimate using the observed standard deviation, largely due to intrinsic variability, one obtains an error, $\Delta_o \tau_a = 0.002$, that is small compared to the calibration uncertainty above.

c. Uncertainty and variation of the aerosol optical properties

Here we examine systematic errors in the determination of τ_a due to the assumptions made about the optical properties of the aerosol, $\omega_0 = 1$, and a single fixed representation of the phase function. These assumptions neglect differences due to varying aerosol composition and particle size distribution. As noted, the uncertainty in the directional scattering coefficient $\Psi = \omega_0 p_a(\Theta_-) \tau_a$ is independent of these assumptions and depends only on how accurately the Rayleigh and surface scattering contributions can be subtracted and on errors introduced by the radiative transfer model approximation.

The single scattering albedo ω_0 varies with aerosol composition and RH but

generally deviates from 1 by well less than 20% in the marine environment (d’Almeida *et al.* 1991). Typical observed values are $0.9 < \omega_0 < 0.999$. The corresponding error in τ_a will be proportional. However, since both ω_0 and $p_a(\Theta_-)$ are determined by the particle size distribution and real and imaginary components of refractive index, we estimate the error in the retrieval of τ_a due to the variation of the product $\omega_0 p_a(\Theta_-)$ by choosing different representative measured size distributions and by varying the imaginary component of the index of refraction, n_i . The two measured size distributions employed for this purpose (Figure 12) bracket the range of continentally influenced to clean maritime conditions (Hoppel *et al.* 1990). n_i was varied from 0, conservative scattering, to 0.008, which corresponds to a single scattering albedo of $\omega_0 = 0.94$. This single scattering albedo is close to the value of $\omega_0 = 0.96$ given by d’Almeida *et al.* (1991) for the “maritime polluted” aerosol type at a wavelength of $0.65 \mu\text{m}$. The $n_i = 0.008$ is also close to the value of $n_i = 0.01$ found by Ignatov *et al.* (1995) to provide the best match between corrected NOAA retrievals of aerosol optical depth and ship-based sun-photometer measurements. The results for the different phase functions are compared to the “conservative NOAA” phase function used in this study (Eq. 12).

Figure 12.

To assess the sensitivity to particle size distribution we evaluated the phase functions corresponding to the particle size distributions of curves 1 and 4 of Figure 8 of Hoppel *et al.* (1990), which are labeled “Continental” and “Marine” in the following discussion. Figure 12 reproduces these size distributions as volume distributions normalized to $1 \text{ particle cm}^{-3}$ together with the distribution from Eq. 12. The corresponding phase functions are shown in Figure 13 together with the “non-conservative NOAA” phase function computed from the size distribution of Eq. 12 but with $n_i = 0.008$.

Figure 13.

Because the scattering angle in the satellite observations varies systematically with latitude and season, the different functional dependencies of the phase functions on scattering angle result in potential systematic errors of the derived latitudinal or

seasonal variation of optical depth. This is illustrated in Figure 14 by plotting the zonal averages of the ratio of the “Marine”, “Continental”, and “non-conservative NOAA” phase functions to the “conservative NOAA” phase function at the observing geometries encountered on July 27 and October 15. This would be the observed variation in the satellite retrieved optical depth if the “true” phase function was given by these other distributions and the retrieval used the “conservative NOAA” phase function.

Near sub-solar latitudes the observed scattering angles are on average close to 180° , where the “non-conservative NOAA” phase function deviates the most from the “conservative” one. At higher latitudes the scattering angle remains below 150° , where the “marine” phase function deviates the most. This pattern follows the sub-solar latitude with season (Figure 14), but will always be centered slightly north of it because of the orbital inclination of NOAA 9, which could result in a systematic north/south bias even in yearly average aerosol optical depth maps.

Figure 14.

If it could be assumed that the Hoppel “continental” and “marine” size distributions bracket the majority of particle size distributions present in the marine environment then the systematic error in aerosol optical depth due to the phase function would be only 5% to 15% (the differences between the curves in Figure 14). However, the size distributions were measured at a constant, below ambient $RH = 55\%$ (J. W. Fitzgerald, *private communication*); variation in both RH and refractive index would increase the variation of phase functions in the real world. For example, increasing the effective radius of the “Marine” size distribution by a factor of two (simulating a high RH condition) increases the relative deviation of the “Continental” from the “Marine” phase function to 25%. The variation of n_i from 0 to 0.008 introduces changes in $\omega_0 p$ of -10% to -20%. Overall, the size distributions and imaginary indices of refraction considered result in systematic errors in the optical depth retrieval using the “conservative NOAA” particle size distribution employed here of up to -40% with an average of about -20%.

d. Radiative transfer approximation

To evaluate the systematic errors introduced by the single scattering approximation and the omission of polarization, we constructed a multiple scattering model lookup table using a version of the doubling and adding radiative transfer code (Hansen and Travis 1974) that includes polarization. The model atmospheric layers were set up analogous to the model used for computing the NOAA operational lookup tables (Rao *et al.* 1989) except that the surface albedo was assumed to be 0 instead of 0.015 in order to isolate the atmospheric radiative transfer effects (polarization and multiple scattering). An aerosol refractive index of 1.5 and particle size distribution given by the modified power law distribution given in Eq. 12 were employed.

The model was used to calculate normalized radiances at the actual cloud-free pixel geometries of the AVHRR observations of October 15 ($0.3 < \mu_0 < 0.76$, $0.44 < \mu < 1$, $0^\circ < \phi < 180^\circ$, $67^\circ < \Theta_- < 180^\circ$) for a range of aerosol optical depths ($0 \leq \tau_m < 1$). Then these theoretical radiances at the satellite viewing geometries were subjected to the single scattering reduction of Section 2. with all the surface terms in Eq. 4 set to 0, and R_R computed without sky reflection ($\rho = 0$), i.e.:

$$R_a = R_m(\tau_m)/T_o - R_R(\rho = 0), \quad (13)$$

where $R_m(\tau_m)$ is the modeled normalized radiance at aerosol optical depth τ_m .

The retrieved optical depth τ_r , using Eq. 11 for the range of viewing geometries, is shown in Figure 15 as a function of the optical depth used as input to the multiple scattering model. The $1\text{-}\sigma$ fractional deviations from the median at each τ_m increase with τ_m from 10% at $\tau_m = 0.1$ to 18% at $\tau_m = 1$ because of multiple scattering effects. A linear fit to the points for $\tau_m < 1$ is given by

$$\tau_r = 0.01 + 1.22\tau_m, \quad (14)$$

with a standard deviation of the residuals of 0.07. The latter quantity is used to

estimate the errors in the optical depth retrieval due to polarization and multiple scattering effects in the atmosphere. For $\tau < 1$ the linear fit suggests a correction of $\tau'_a = 0.82(\tau_a - 0.01)$ to the retrieval of Eq. 11 for the ensemble average of all retrievals on 1986 October 15.

Figure 15.

In a detailed analysis of the treatment of Rayleigh scattering in radiative transfer models, Gordon *et al.* (1988) found that neglecting multiple scattering and polarization introduces errors in the order of -6% for channel 1. This decrease in R_R would result in an increase of τ_a by $+0.005$ to $+0.02$, median $+0.016$, consistent with the median $\tau_r = 0.012$ for $\tau_m = 0$ determined here from the data in Figure 15.

e. Surface scattering processes

In areas near the continental margins a small but finite contribution of light scattered by pigments suspended in the top layer of the ocean could result in large errors in τ_a , particularly near nadir. For instance, Hovis *et al.* (1980) measured upwelling spectral radiances up to $L_{ss} = 5 \text{ W m}^{-2} \mu\text{m}^{-1} \text{ sr}^{-1}$ in the channel 1 wavelength range (Chesapeake Bay and Gulf of Mexico). With the integrated solar spectral irradiance, weighted by the spectral response function of channel 1, $F_1 = 191.3 \text{ W m}^{-2}$, and the equivalent width of the spectral response function $W_1 = 0.117 \mu\text{m}$ (Kidwell 1995, Table 3.3.2-2), this radiance corresponds to a normalized radiance $R_{ss} = \pi W_1 L_{ss} / F_1 \sim 0.01$ and a median apparent optical depth increase $\Delta_{ss} \tau_a \sim +0.06$. However, these areas can be flagged in the final optical depth map using the monthly mean pigment concentrations from the CZCS (Feldman *et al.* 1989). For lowest pigment concentrations reported in their study area (0.09 mg m^{-3} and 0.35 mg m^{-3}), Hovis *et al.* (1980) found radiances of $L_{ss} \sim 0.3 \text{ W m}^{-2} \mu\text{m}^{-1} \text{ sr}^{-1}$, which correspond to $\Delta_{ss} \tau_a \sim +0.004$. Ignatov *et al.* (1995), based on data for “case 1” water (pigment concentration $C_p < 0.25 \text{ mg m}^{-3}$) by Morel and Prieur (1977) and Gordon and Morel (1983), estimated a globally

representative reflectivity $\rho_{ss} = R_{ss}/\mu_0 = 0.0014 \pm 0.0006$ for the AVHRR channel 1. This $\Delta\rho_{ss} = 0.0006$ corresponds to a random error in aerosol optical depth of $\Delta_{ss}\tau_a = 0.002$.

Sea foam can produce a signature of the same magnitude, $R_f \sim 0.01$, where the surface wind speed exceeds 15 m/s (Gregg and Carder 1990). Using the ECMWF wind data to evaluate Eq. 8 we found the average sea foam radiance to be quite low $R_f \sim 0.0003$ with a standard deviation of 0.0005, and the maximum for 1986 October 15 reached $R_f = 0.006$. The standard deviation of the predicted sea foam contribution is used to estimate the systematic error due to sea foam at $\Delta_f\tau_a = 0.007$. Notice however that this is only an expected error for average wind speed conditions. In areas of high surface wind speed and poor data constraints on the ECMWF analyzed wind fields, for instance the high southern latitudes, the error due to the sea foam radiance can be much larger (up to $\Delta_f\tau_a = 0.07$ for $\Delta W = 15$ m/s).

The error due to residual sunglint contamination is estimated from the sunglint exclusion cutoff of $R_s = 5 \cdot 10^{-5}$ and the disappearance of any discernible bias in Figure 3 below that threshold. The threshold corresponds to an error in optical depth of $\Delta_s\tau_a = 0.0007$.

f. Atmospheric transmission

In Eq. 4 the surface terms above are multiplied by the tropospheric transmission due to aerosol and Rayleigh scattering, $T_a T_R$. The uncertainty in this product is dominated by the assumption of a constant aerosol optical depth of $\tau_a = 0.2$ to avoid having to iterate the aerosol retrieval. However, since the surface terms are all small, the error introduced by that assumption is small as well. Using the retrieved aerosol optical depth for October 15, τ_a , to evaluate the error that is proportional to $T_a(\tau_a) - T_a(0.2)$, we find a mean bias of +0.001 and standard deviation $\Delta_T\tau_a = 0.003$.

g. Error budget summary

The various sources of random and systematic errors in aerosol optical depth derived from AVHRR GAC data are summarized in Table 4. They are grouped according to the sub-sections of this section. “Systematic” errors refer to uncertainties in the retrieved optical depth that could systematically bias the result one way or another, but not necessarily in a predictable way. “Random” errors refer to uncertainties whose sign changes rapidly (e.g. within one grid cell) and therefore whose net effect is expected to approach zero in averages over large enough samples. “Absolute” errors are in “units” of optical depth and are nearly independent of optical depth. “Relative” errors are approximately proportional to optical depth and are therefore given in percent.

Table 4.

For a typical grid cell that contains $N = 50$ points and has an average optical depth of $\tau_a = 0.25$ the various sources of random errors combine (using the square-root of the sum of squares of the errors in columns 4 and 5 of Table 4) to $\overline{\Delta_r \tau_a} = 0.03$. Taking a straight sum of the signed errors in columns 2 and 3, one obtains a net bias of $\Delta_s \tau_a = +0.02^{+0.06}_{-0.05}$.

6. Summary

A method of retrieval of vertical aerosol optical depth τ_a at $0.64 \mu\text{m}$ from AVHRR GAC data has been described that allows comparison to sulfate column burdens predicted from a transport and transformation model (GChM-O). The random and systematic errors have been estimated (Table 4). For a grid cell average optical depth of $\tau_a = 0.25$ the uncertainty due to detector noise and due to lack of knowledge or approximation errors of the relevant scattering processes is $\Delta\tau \sim 0.02$. The single scattering approximation to the radiative transfer calculation introduces errors of 0.03 and biases of -0.03 to +0.08. Assumptions about the microphysical properties of the aerosol introduce systematic errors that vary with latitude and season.

Because of these limitations, the aerosol optical depth derived from the AVHRR GAC data is most suitable for examining aerosol events of high optical depth. That means it is suitable for instantaneous comparison of the amplitude and location of aerosol plumes with model predictions that are based on actual meteorological conditions at and immediately preceding the time of observation.

Since the largest uncertainties are due to the heavy reliance on modeled radiances, we can expect significant improvements with future satellite instruments when these model dependencies can be reduced, e.g. through the use of multiple narrow-band visible channels, multiple viewing angles, and polarization (Penner *et al.* 1994; Hansen *et al.* 1993).

Acknowledgments. We thank Jim Coakley (Oregon State University) for providing a program to read NOAA GAC data. The AVHRR GAC data for 1986 October were provided by Compton Tucker of NASA/Goddard Space Flight Center. The data for 1986 July were obtained from NOAA/NESDIS. The many constructive comments of an anonymous referee greatly improved this manuscript. This research was supported by the Environmental Sciences Division of the U.S. Department of Energy (DOE) as part of the Atmospheric Radiation Measurement Program and was performed under the auspices of DOE under Contract No. DE-AC02-76CH00016.

References

- Benkovitz, C. M., C. M. Berkowitz, R. C. Easter, S. Nemesure, R. Wagener and S. E. Schwartz, 1994: Sulfate over the North Atlantic and adjacent continental regions: Evaluation for October and November, 1986 using a three-dimensional model driven by observation-derived meteorology. *J. Geophys. Res.*, **99**, 20725–20756.
- Berkowitz, C. M., S. J. Ghan, C. M. Benkovitz, R. Wagener, S. Nemesure and S. E. Schwartz, 1994: Evaluation of sulfate aerosol optical depths over the North Atlantic and comparison with satellite observations. *Proc. Conference on Atmospheric Chemistry, 74th AMS Annual Meeting*, Nashville, Tennessee, American Meteorological Society, 154–160.
- Boucher, O. and T. L. Anderson, 1995: GCM assessment of the sensitivity of direct climate forcing by anthropogenic sulfate aerosols to aerosol size and chemistry. *J. Geophys. Res.*, **100**, 26117–26134.
- Charlson, R. J., J. Langner, H. Rodhe, C. B. Leovy and S. G. Warren, 1991: Perturbation of the northern hemisphere radiative balance by backscattering from anthropogenic sulfate aerosols. *Tellus*, **43A**, 152–163.
- Charlson, R. J., S. E. Schwartz, J. M. Hales, R. D. Cess, J. A. Coakley, Jr., J. E. Hansen and D. J. Hofmann, 1992: Climate forcing by anthropogenic aerosols. *Science*, **255**, 423–430.
- Cleveland, W., 1979: Robust locally weighted regression and smoothing scatterplots. *J. of the American Statistical Association*, **74**, 829–836.
- Cox, C. and W. Munk, 1956: Slopes of the sea surface deduced from photographs of sun glitter. *Bull. Scripps Inst. Oceanogr. Univ. Calif.*, **6**, 401–488.
- d’Almeida, G. A., P. Koepke and E. P. Shettle, 1991: *Atmospheric Aerosols: Global Climatology and Radiative Characteristics*. A. Deepak Publishing.
- Durkee, P. A., F. Pfeil, E. Frost and R. Shema, 1991: Global analysis of aerosol particle characteristics. *Atmospheric Environment*, **25A**, 2457–2471.

- European Centre for Medium-Range Weather Forecasts, Research Department, 1988: ECMWF Forecast Model: Adiabatic Part. Research Manual 2nd edn.
- Feldman, G., N. Kuring, C. Ng, W. E. Esaias, C. McClain, J. Elrod, N. Maynard, D. Endres, R. Evans, J. Brown, S. Walsh, M. Carle and G. Podesta, 1989: Ocean color: Availability of the global data set. *Eos, Trans. Amer. Geophys. Un.*, **70**, 634–641.
- Gordon, H. R. and A. Y. Morel, 1983: *Remote Assessment of Ocean Color for Interpretation of Satellite Visible Imagery: A Review*. Lecture Notes on Coastal and Estuarine Studies, Vol. 4, Springer-Verlag.
- Gordon, H. R., J. W. Brown and R. H. Evans, 1988: Exact Rayleigh scattering calculations for use with the Nimbus-7 Coastal Zone Color Scanner. *Appl. Opt.*, **27**, 862–871.
- Gregg, W. W. and K. L. Carder, 1990: A simple spectral solar irradiance model for cloudless maritime atmospheres. *Limnol. Oceanogr.*, **35**, 1657–1675.
- Guimaraes, P. T. and R. McPeters, 1990: TOMS gridded ozone data 1978–1988. CD-ROM, NASA Goddard Space Flight Center. [Version 6.0, data provided by Goddard Ozone Processing Team].
- Hansen, J. and L. Travis, 1974: Light scattering in planetary atmospheres. *Space Sci. Rev.*, **16**, 527–610.
- Hansen, J., W. Rossow and I. Fung (eds), 1993: *Long-Term Monitoring of Global Climate Forcings and Feedbacks*, NASA Conference Publication, Vol. 3234, NASA Goddard Institute for Space Studies, New York. [Workshop held 1992 February 3-4].
- Hoppel, W. A., J. W. Fitzgerald, G. M. Frick and R. E. Larson, 1990: Aerosol size distributions and optical properties found in the marine boundary layer over the Atlantic Ocean. *J. Geophys. Res.*, **95**, 3659–3686.
- Houghton, J. T., B. A. Callander and S. K. Varney (eds), 1992: *Climate Change 1992: The Supplementary Report to the IPCC Scientific Assessment*. Cambridge University Press. [Working Group I of the Intergovernmental Panel on Climate Change (IPCC), World Meteorological Office, United Nations Environmental Programme].

- Houghton, J. T., L. G. Meira Filho, J. Bruce, H. Lee, D. A. Callander, E. Haipes, N. Harris and K. Maskell (eds), 1994: *Climate Change 1994: Radiative Forcing of Climate Change and an Evaluation of the IPCC 1992 Emission Scenarios*. Cambridge University Press. [Working Groups I and III of the Intergovernmental Panel on Climate Change (IPCC), World Meteorological Office, United Nations Environmental Programme].
- Hovis, W. A., D. K. Clark, F. Anderson, R. W. Austin, W. H. Wilson, E. T. Baker, D. Ball, H. R. Gordon, J. L. Mueller, S. Z. El-Sayed, B. Sturm, R. C. Wrigley and C. S. Yentsch, 1980: Nimbus-7 Coastal Zone Color Scanner: System description and initial imagery. *Science*, **210**, 60–63.
- Husain, L. and V. A. Dutkiewicz, 1990: A long-term (1975–1988) study of atmospheric SO_4^{2-} : Regional contributions and concentration trends. *Atmospheric Environment*, **24A**, 1175–1187.
- Ignatov, A. M., L. L. Stowe, S. M. Sakerin and G. K. Korotaev, 1995: Validation of the NOAA/NESDIS satellite aerosol product over the North Atlantic in 1989. *J. Geophys. Res.*, **100**, 5123–5132.
- Inn, E. and Y. Tanaka, 1953: Absorption coefficient of ozone in the ultraviolet and visible regions. *J. Opt. Soc. Am.*, **43**, 870–873.
- Kaufman, Y. J. and B. N. Holben, 1993: Calibration of the AVHRR visible and near-IR bands by atmospheric scattering, ocean glint and desert reflection. *Int. J. Remote Sensing*, **14**, 21–52.
- Kidwell, K. B., 1995: NOAA Polar Orbiter Data Users Guide. National Oceanic and Atmospheric Administration, National Environmental Satellite, Data, and Information Service; National Climatic Data Center; Satellite Data Services Division, Washington, D.C.
- Kiehl, J. T. and B. P. Briegleb, 1993: The relative roles of sulfate aerosols and greenhouse gases in climate forcing. *Science*, **260**, 311–314.
- Koepke, P., 1984: Effective reflectance of oceanic whitecaps. *Appl. Opt.*, **23**, 1816–1824.

- Langner, J. and H. Rodhe, 1991: A global three-dimensional model of the tropospheric sulfur cycle. *J. Atmos. Chem.*, **13**, 225–263.
- Langner, J., T. S. Bates, R. J. Charlson, A. D. Clark, P. A. Durkee, J. Gras, J. Heintzenberg, D. J. Hofmann, B. Huebert, C. Leck, J. Lelieveld, J. A. Ogren, J. Prospero, P. K. Quinn, H. Rodhe and A. G. Ryaboshapko, 1993: The global atmospheric sulfur cycle: An evaluation of model predictions and observations. Report CM-81, Department of Meteorology, Stockholm University, International Meteorological Institute, Stockholm.
- Morel, A. and L. Prieur, 1977: Analysis of variations in ocean color. *Limnol. Oceanogr.*, **22**, 709–722.
- Nemesure, S., R. Wagener and S. E. Schwartz, 1995: Direct shortwave forcing of climate by anthropogenic sulfate aerosol: Sensitivity to particle size, composition, and relative humidity. *J. Geophys. Res.*, **100**, 26105–26116.
- Penner, J. E., R. J. Charlson, J. M. Hales, N. S. Laulainen, R. Leifer, T. Novakov, J. Ogren, L. F. Radke, S. E. Schwartz and L. Travis, 1994: Quantifying and minimizing uncertainty of climate forcing by anthropogenic aerosols. *Bull. Amer. Meteorol. Soc.*, **75**, 375–400.
- Rao, C. R. N., 1987: Pre-launch calibration of channels 1 and 2 of the Advanced Very High Resolution Radiometer. NOAA Technical Report NESDIS 36, National Oceanic and Atmospheric Administration, Washington, D.C.
- Rao, C. R. N., J. Chen, F. Staylor, P. Abel, Y. Kaufman, E. Vermote, W. Rossow and C. Brest, 1993: Degradation of the visible and near-infrared channels of the Advanced Very High Resolution Radiometer on the NOAA-9 spacecraft: Assessment and recommendations for corrections. NOAA Technical Report NESDIS 70, National Oceanic and Atmospheric Administration, Washington, D.C.
- Rao, C. R. N., L. L. Stowe and E. P. McClain, 1989: Remote sensing of aerosols over the oceans using AVHRR data: Theory, practice, and applications. *Int. J. Remote Sensing*, **10**, 743–749.

- Schwartz, S. E., 1996: The Whitehouse Effect – Shortwave radiative forcing of climate by anthropogenic aerosols: An overview. *J. Aerosol Sci.*, **27**, 359–382.
- Stowe, L. L., R. M. Carey and P. P. Pellegrino, 1992: Monitoring the Mt. Pinatubo aerosol layer with NOAA 11 AVHRR data. *Geophys. Res. Lett.*, **19**, 159.
- Taylor, K. E. and J. E. Penner, 1994: Climate system response to aerosols and greenhouse gases: A model study. *Nature*, **369**, 734–737.

Figure Captions

Figure 1. The scattering geometry for the radiative processes considered in Table 1. For simplicity, the azimuth ϕ is not shown. The foam radiance R_f and the subsurface scattering R_{ss} are assumed to be isotropic.

Figure 2. Histogram of pixels according to the radiance ratio of channel 1 to channel 2, S_{12} , for 76 oceanic scenes of the 1986 July 24 NOAA 9 data. Only the unshaded pixels between the vertical lines at $S_{12} = 1.5$ and $S_{12} = 3.5$ are considered potentially cloud free. Note log scale.

Figure 3. Dependence of aerosol contribution to normalized path radiance on computed sunglint radiance. *Points and Box-whiskers:* Normalized radiance due to aerosol scattering R_a as a function of the logarithm of the normalized radiance due to sunglint. Each point indicated by the intersection of vertical and horizontal “whiskers” represents the median of 360 grid cells sorted by R_s . The boxes enclose 68% or 245 grid cells and the whiskers extend to 95% or 342 grid cells. *Solid line:* Identity. *Dashed line:* Sunglint cut-off chosen to eliminate points with apparent residual bias due to sunglint for $R_s > 5 \cdot 10^{-5}$.

Figure 4. Observed and modeled radiances for a single scan of NOAA 9 AVHRR GAC channel 1 data in the western North Atlantic for 1986 July 27 and successive elimination of data points according to the several screening tests. Scan direction is east to west. *Solid line with symbols:* Observed radiance. *Plus symbols:* Pixels failing each of the four screening tests of Section 3. (Panels a – d). In each successive panel the pixels that have been previously rejected are left blank. *Dotted line:* Sum of normalized Rayleigh and sky radiances. *Dashed line:* *Dotted line* plus sea foam radiance. *Solid line:* *Dashed line* plus sunglint radiance. *Panel e:* Net normalized radiance, presumed to be due to aerosol scattering, of those points that pass all screening tests. Adjacent points are connected. Note increasingly expanding scale in going from top to bottom (Panel a to e).

Figure 5. Same as Figure 4 for 1986 October 15. The *dotted line* is indistinguishable from the *dashed line* because the calculated sea foam radiance is negligible in this particular scan.

Figure 6. Aerosol vertical optical depth at $0.64 \mu\text{m}$, averaged over $1.125^\circ \times 1.125^\circ$ grid cells, for *a)* 1986 July 27 and *b)* 1986 October 15.

Figure 7. Grid cell average ($1.125^\circ \times 1.125^\circ$) aerosol vertical optical depth at $0.64 \mu\text{m}$, τ_a , *vs.* the cosine of the solar zenith angle, μ_0 . Each point indicated by the intersection of vertical and horizontal “whiskers” represents the median of 360 grid cells sorted by μ_0 . The boxes enclose 68% or 245 grid cells and the whiskers extend to 95% or 342 grid cells. The data to the left of the *dashed line* are eliminated from further analysis, as explained in the text.

Figure 8. Box-whisker plot of standard deviation *vs.* the mean aerosol vertical optical depth at $0.64 \mu\text{m}$ of each of the 5,051 $1.125^\circ \times 1.125^\circ$ grid cells for October 15, that contain at least 2 pixels. Each point indicated by the intersection of vertical and horizontal “whiskers” represents the median of 360 grid cells sorted by optical depth. The boxes enclose 68% or 245 grid cells and the whiskers extend to 95% or 342 grid cells.

Figure 9. Scatterplot of aerosol vertical optical depth at $0.64 \mu\text{m}$ *vs.* latitude. Left panel: 1986 July 27 (Longitude range 100°W to 150°E ; see Figure 6). *Right panel:* 1986 October 15 (global coverage in longitude). *Solid line:* Locally Weighted Scatterplot Smoothing curve (Cleveland 1979).

Figure 10. Aerosol vertical optical depth at $0.64 \mu\text{m}$ in the Barents Sea (latitude $66^\circ - 72^\circ$) for 1986 July 27. Different symbols represent the median in each longitude bin from five consecutive orbits (spaced 100 minutes apart). The mean local times for the sequence are: “+” 7:16, “*” 9:00, “◊” 10:39, “△” 12:20, “□” 13:52. The *whiskers* extend to 68% of the data in each longitude bin.

Figure 11. Aerosol vertical optical depth at $0.64 \mu\text{m}$ derived from AVHRR GAC data using the recommended correction for the post-launch sensitivity degradation (Rao *et al.*, 1993) for 1986 October 15 *vs.* the optical depth derived using the operational calibration. Solid line denotes one-to-one line.

Figure 12. Volume distributions normalized to 1 particle cm^{-3} . \times : “Marine” distribution from curve 4 of Figure 8 of Hoppel *et al.* (1990). \diamond : “Continental” distribution from curve 1 of Figure 8 of Hoppel *et al.* (1990). *Thick line*: “NOAA” distribution from Eq. 12 (Rao *et al.* 1989). Note logarithmic scale on ordinate.

Figure 13. The product of the Mie scattering phase function p and the single scattering albedo ω_0 as a function of scattering angle Θ_- for: *Thick solid line*: “NOAA” particle size distribution (refractive index $n_r = 1.5$, $n_i = 0$); *Thin solid line*: “NOAA” particle size distribution but with refractive index $n_r = 1.5$, $n_i = 0.008$, giving $\omega_0 = 0.94$; *dot-dashed line*: “Marine” particle size distribution ($n_r = 1.43$, $n_i = 0$) interpolated with a fourth degree polynomial in $\log(dn/dr)$ vs. $\log(r)$; *dotted line*: “Continental” size distribution ($n_r = 1.43$, $n_i = 0$) interpolated with a fourth degree polynomial in $\log(dn/dr)$ vs. $\log(r)$.

Figure 14. Zonal average ratios of $\omega_{0,i}p_i$ for i being either “Marine” (*dot-dashed line*), “Continental” (*dotted line*), or “non-conservative NOAA” ($n_i = 0.008$, *solid line*) phase functions to $\omega_0 p$ for the “conservative NOAA” phase function (Figure 13) evaluated at the satellite observing geometries applicable to 1986 July 27 (*left panel*) and 1986 October 15 (*right panel*).

Figure 15. Aerosol vertical optical depth at $0.64 \mu\text{m}$ retrieved with Eq. 11 from normalized radiances computed with a multiple scattering model (see text) for the actual AVHRR NOAA 9 observing geometries of 1986 July 27. At each model input τ_m the $+$ symbol marks the median τ_r over all retrievals (different geometries), the box includes 68% and the “whiskers” 95% of the retrievals. *Dotted line*: Identity. *Solid line*: Linear fit to all points $\tau_m < 1$.

Tables

Layer	Processes	Typical Radiative Effect
Stratosphere	Ozone Absorption	$T_o \sim 0.9$ to 0.95
Troposphere	Rayleigh scattering	$R_R \sim 0.01$ to 0.05
		$T_R \sim 0.8$ to 0.9
	Aerosol scattering	$R_a \sim 0.$ to 0.1
		$T_a \sim 0.1$ to $1.$
Ocean Surface	Sunglint	$R_s \sim 0.$ to 0.2
	Foam	$R_f \sim 0.$ to 0.012
	Subsurface scattering	$R_{ss} \sim 0.$ to 0.0006

Table 1. Radiative processes in the atmosphere-ocean system: The radiative effects are the modeled ranges, as described in Section 2., for 1986 July 27 in a $(2000 \text{ km})^2$ region centered in the North Atlantic and can be considered typical for mid-latitude summer. They are given here as a measure of the relative importance of each process. T_o refers to the direct transmission of the ozone layer; subscripted R s are normalized radiances for a given scattering process.

Channel	Spectral band	λ_{eff}	τ_R
	$[\mu\text{m}]$	$[\mu\text{m}]$	
1	0.58–0.70	0.64	0.053
2	0.70–1.00	0.83	0.019

Table 2. NOAA-9 AVHRR channel spectral bands. Source: Kidwell (1995). The effective wavelength λ_{eff} is defined by $\int T_f(\lambda)\lambda d\lambda / \int T_f(\lambda)d\lambda$, where $T_f(\lambda)$ is the channel transmission function. The Rayleigh scattering optical depth, τ_R , is computed with Eq. 6 at $\lambda = \lambda_{eff}$.

Test	Fraction of pixels, % median(range)
S_{12} Threshold	75(40–100)
Spatial Uniformity	10(0–40)
Distancing	3(0–15)
High Sunlint	5(0–8)
$\mu_0 < 0.3$	0.4(0–1)
“uncontaminated”	7(0–20)

Table 3. Percentage of pixels of each scene (384×512 pixels) failing each cloud free test; median and range for 70 scenes on 1986 July 27.

Quantity	Systematic Error		Random Error	
	Absolute	Relative[%]	Absolute	Relative[%]
R	0.01^a	5^b	$0.014N^{-1/2}{}^c$	
T_o			0.002	
$\omega_0 p_a$		-20		
$R_a(\text{model})$	+0.01	+22		10 to 18 ^d
R_{ss}	0.000 ^e		0.002	
R_f			0.007 ^f	
R_s			0.0007	
$T_a T_R$	+0.001		0.003	

^adue to AVHRR absolute calibration uncertainty of 5%

^bfor $\tau_a > 0.2$

^cSince this is the contribution due to random detector noise the expected error of the grid cell mean will decrease as $N^{-1/2}$, where N is the number of pixels included in the grid cell average (range 1 to 1125, typically 10 to 100, median 50, mean 124)

^ddependent on optical depth: 10% at $\tau_a = 0.1$ to 18% at $\tau_a = 1$

^eup to +0.06 in areas of high pigment concentrations, e.g. continental shelves

^flarger errors up to 0.07 at high southern latitudes

Table 4. Summary of systematic and random errors in the aerosol optical depth retrieval. Signed numbers are biases in the sense of “retrieved” minus “true” optical depth; numbers without a sign can go either way.

Figures

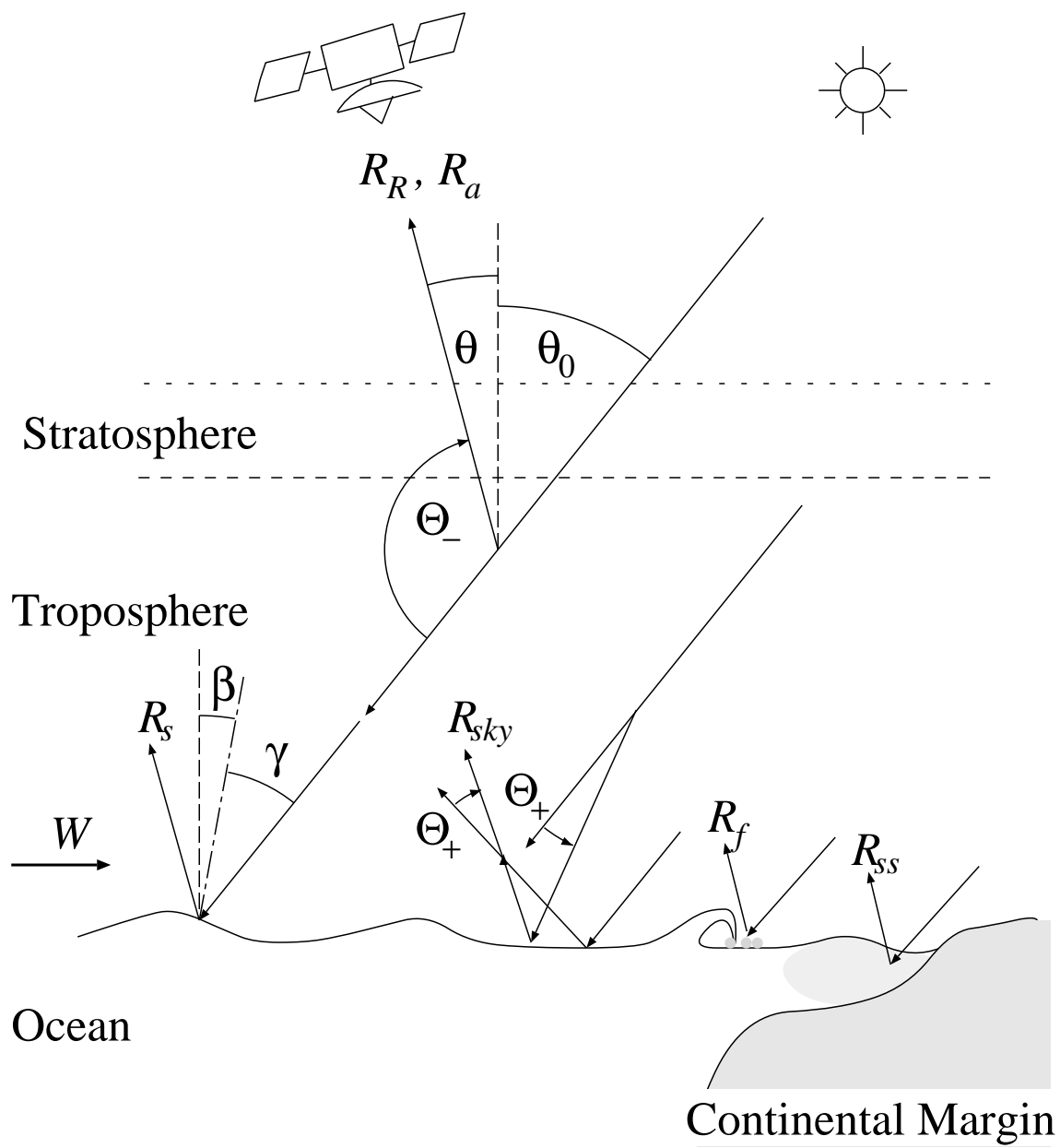


Figure 1.

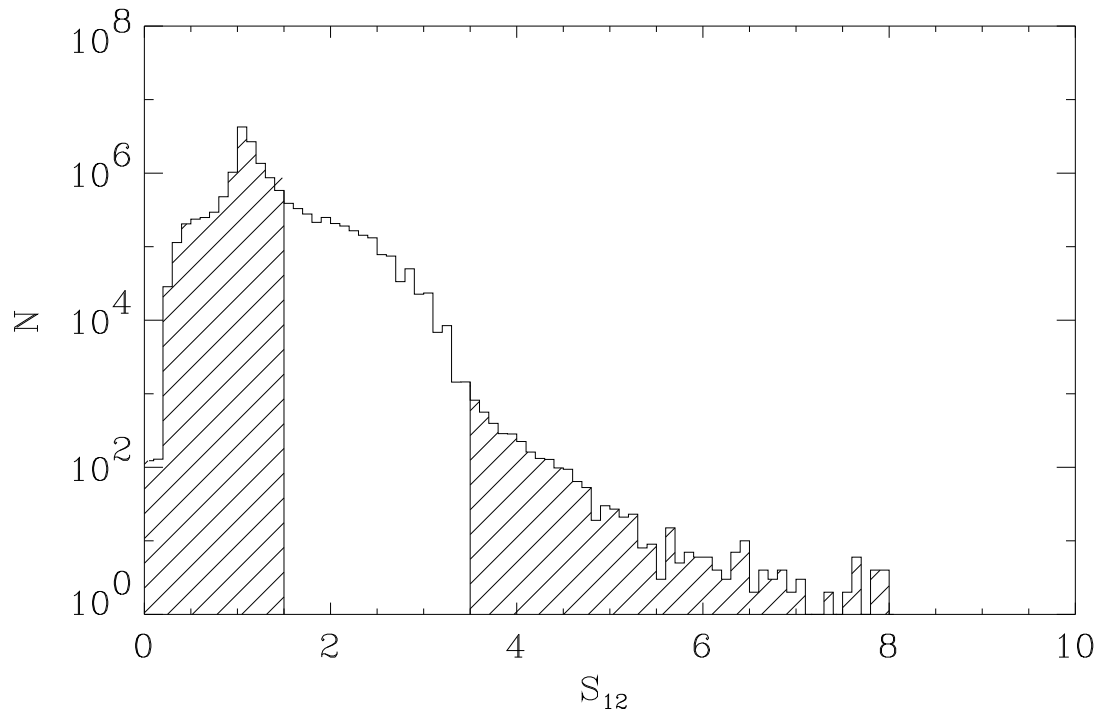


Figure 2.

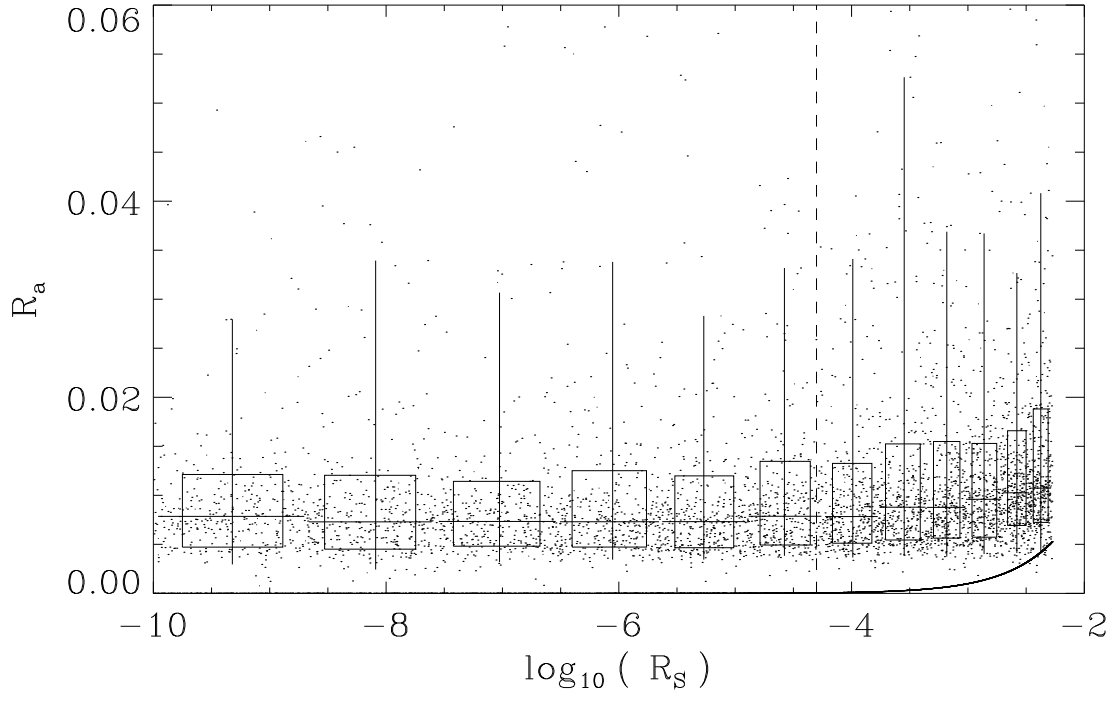


Figure 3.

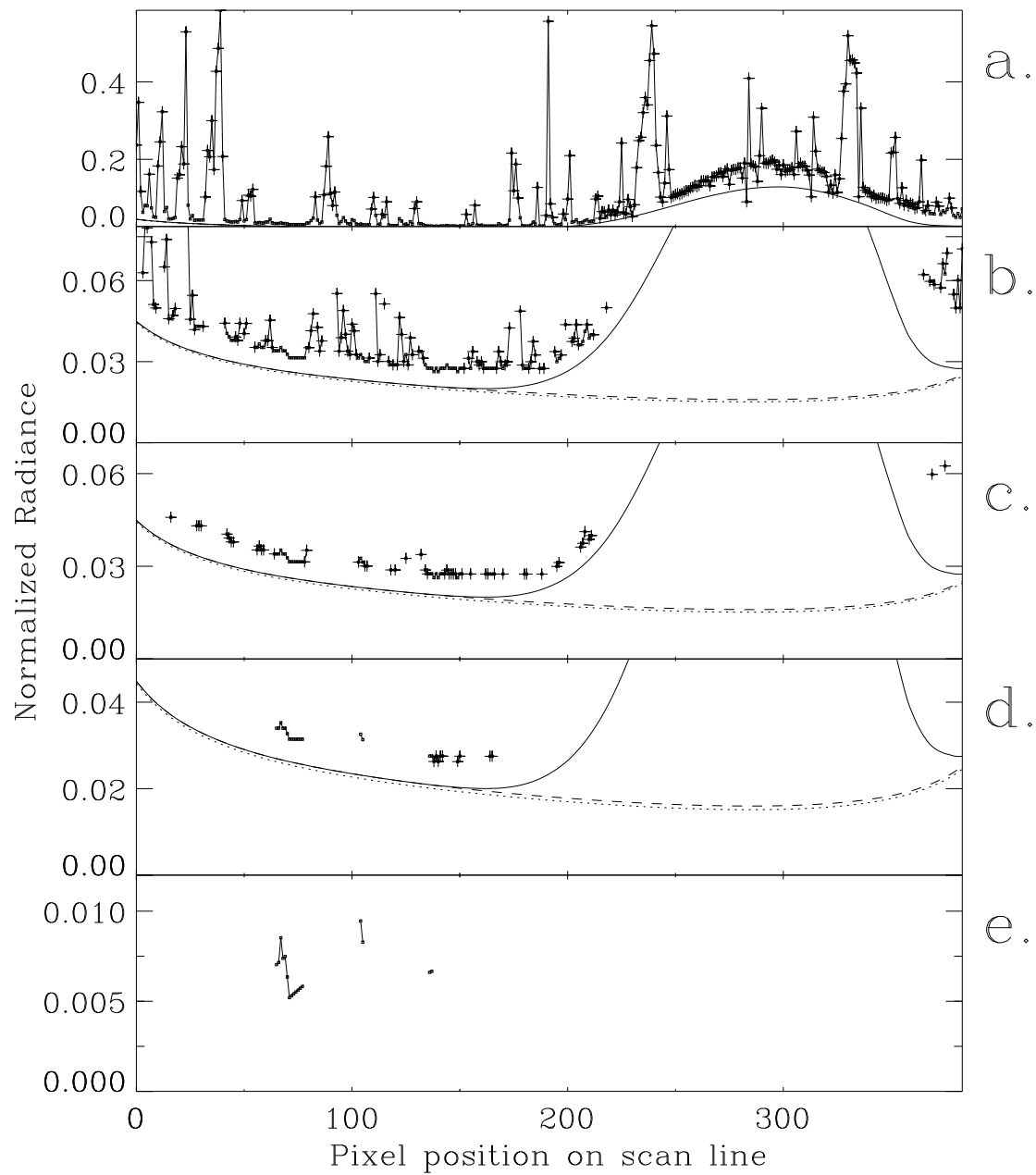


Figure 4.

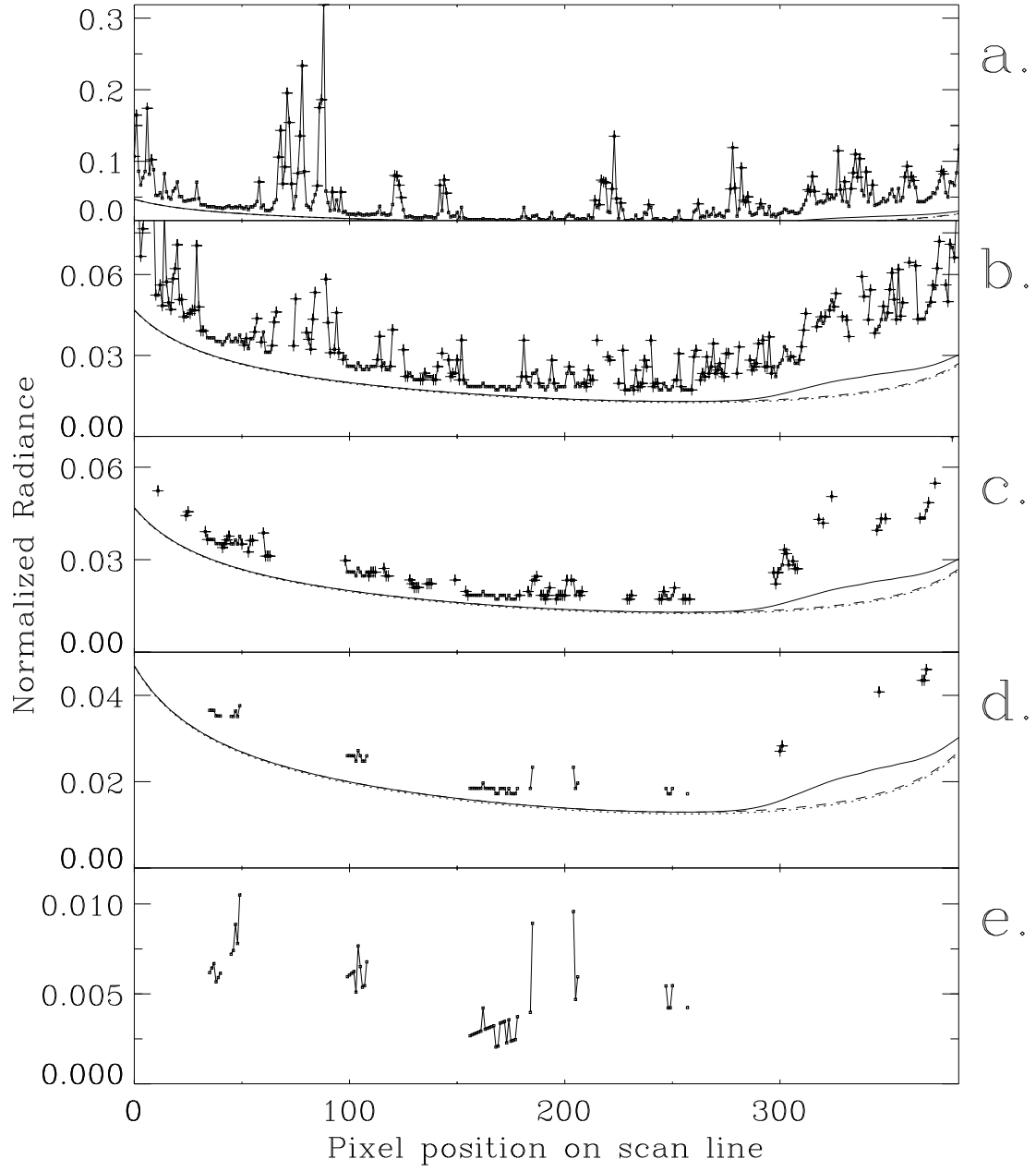
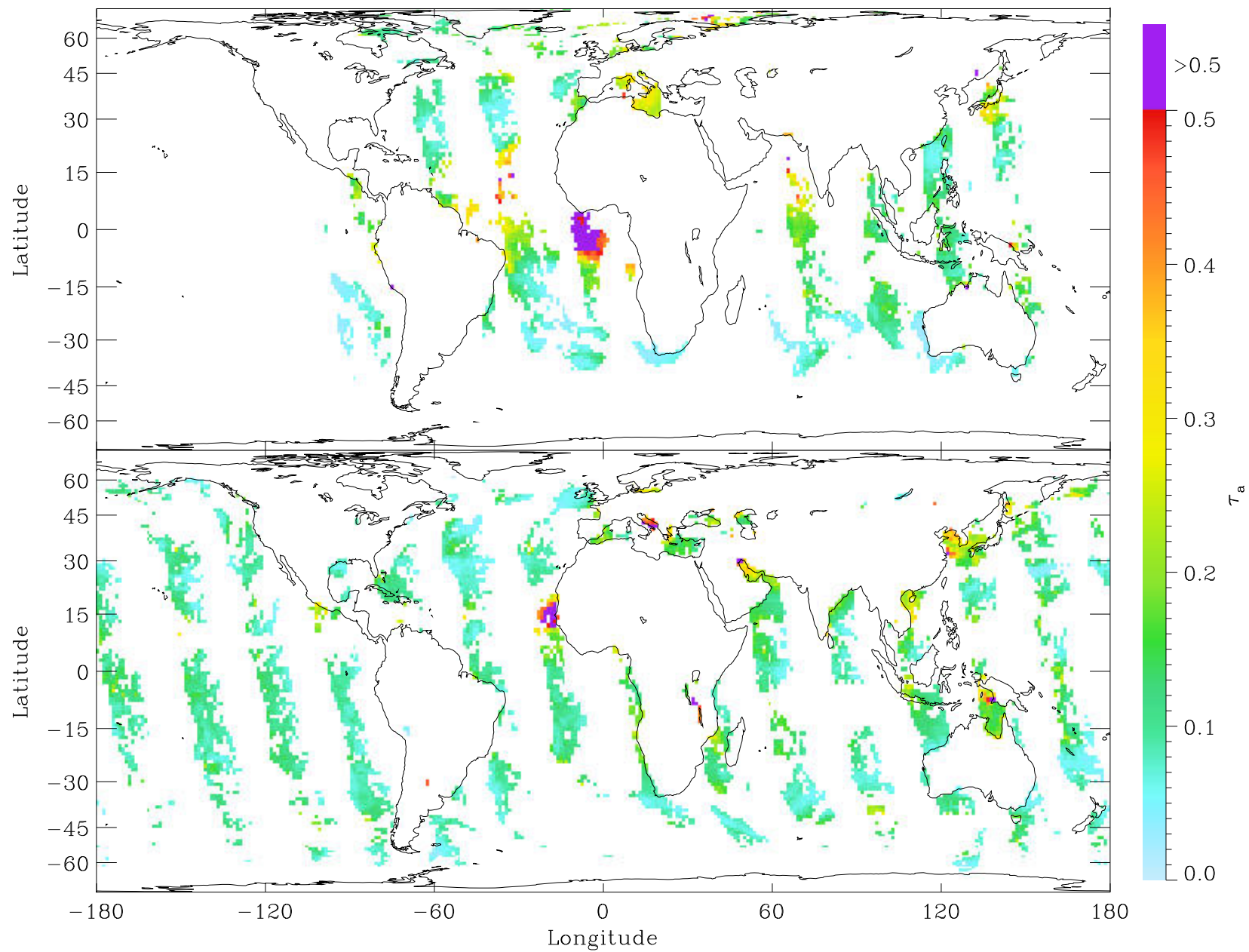


Figure 5.



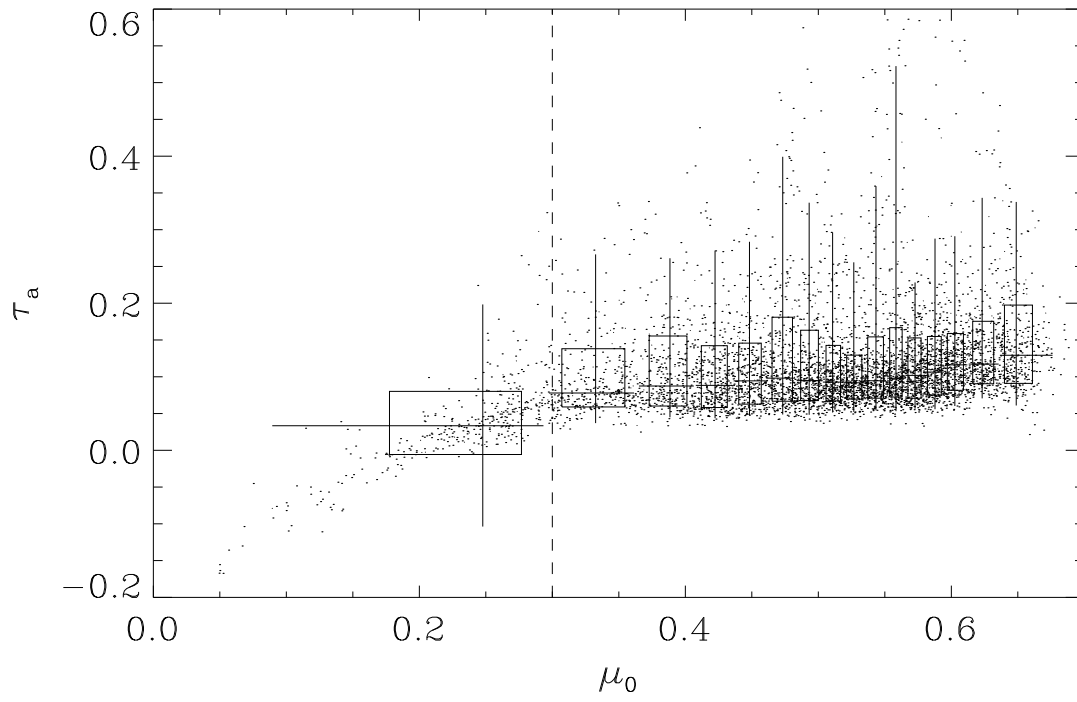


Figure 7.

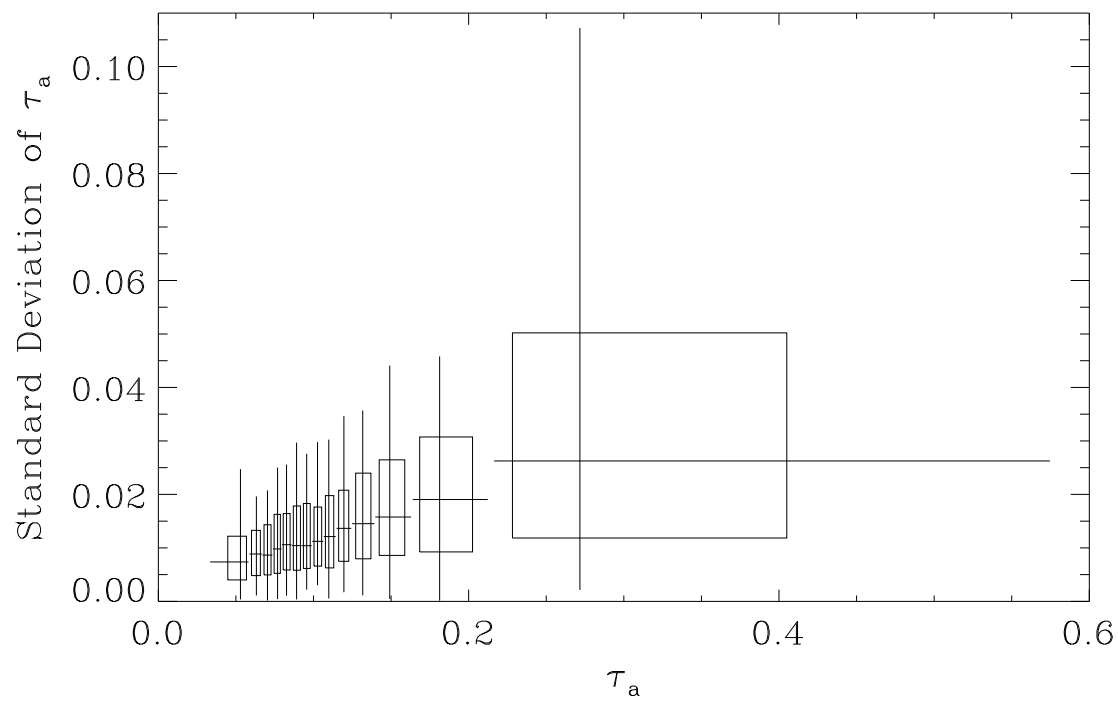


Figure 8.

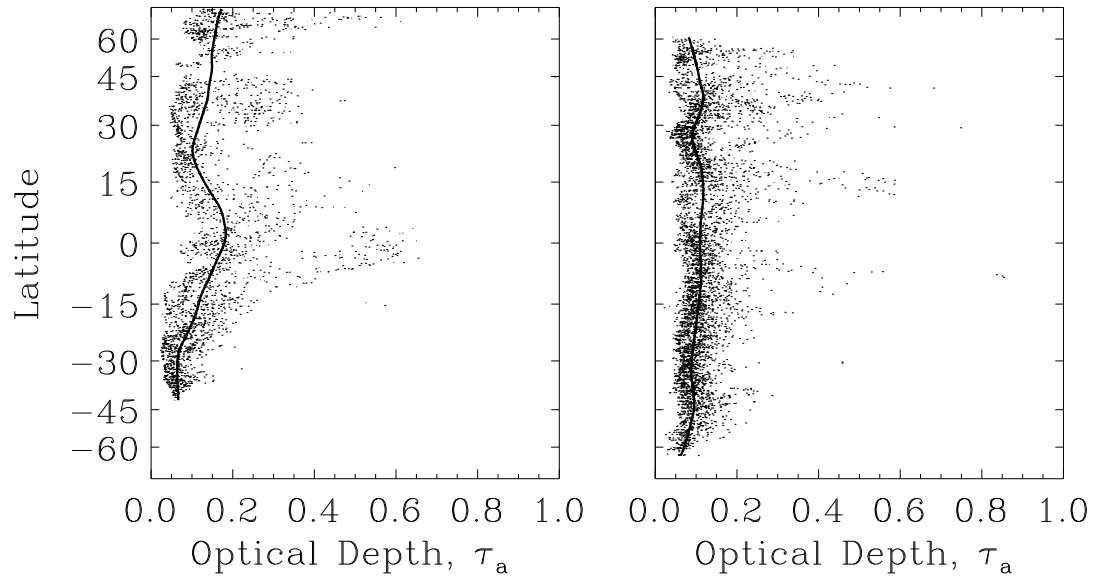


Figure 9.

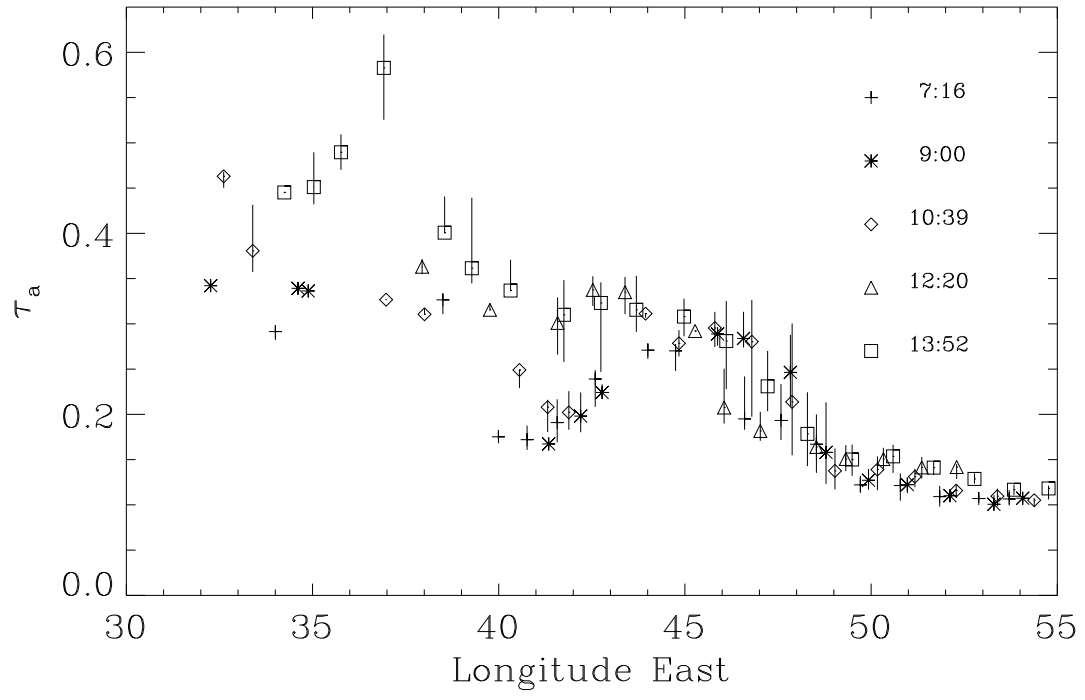


Figure 10.

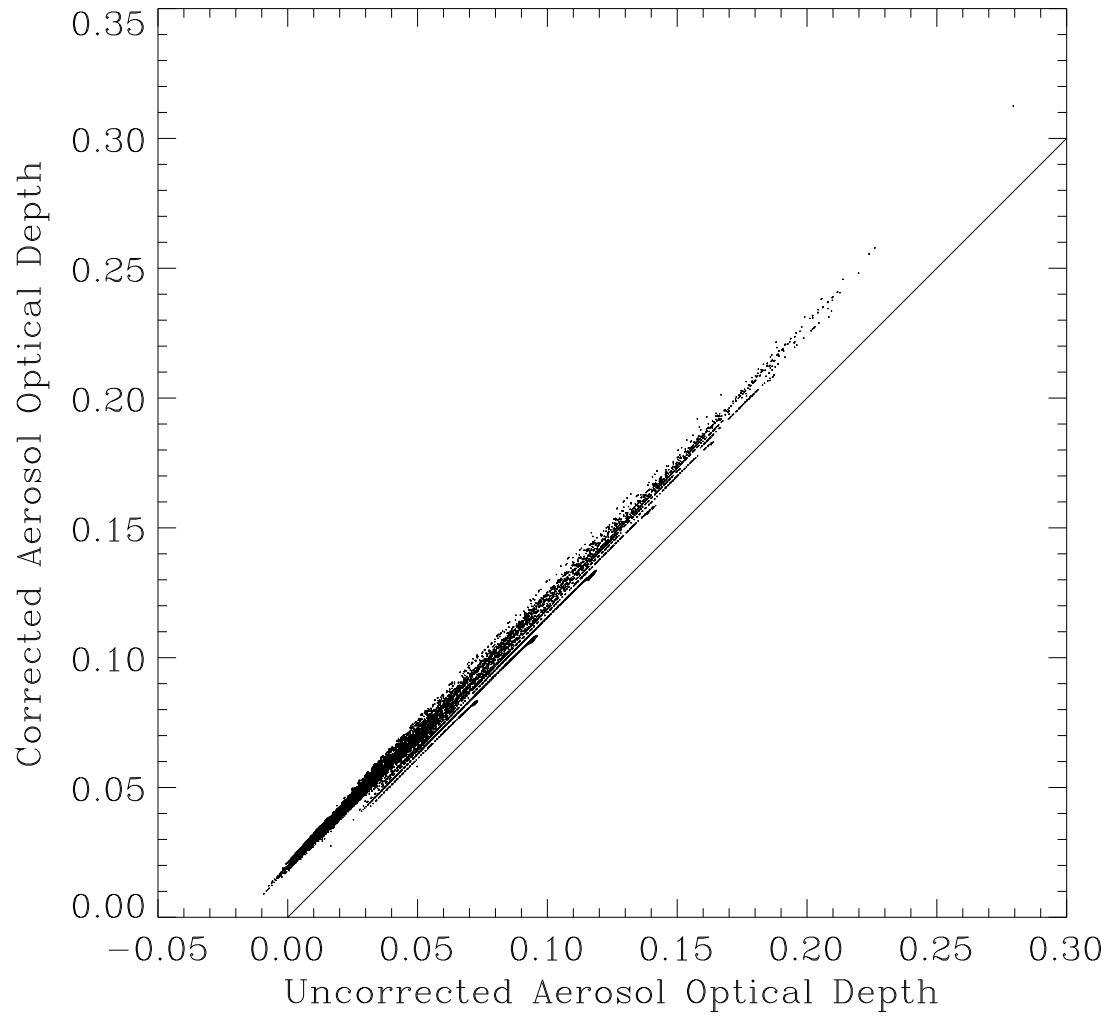


Figure 11.

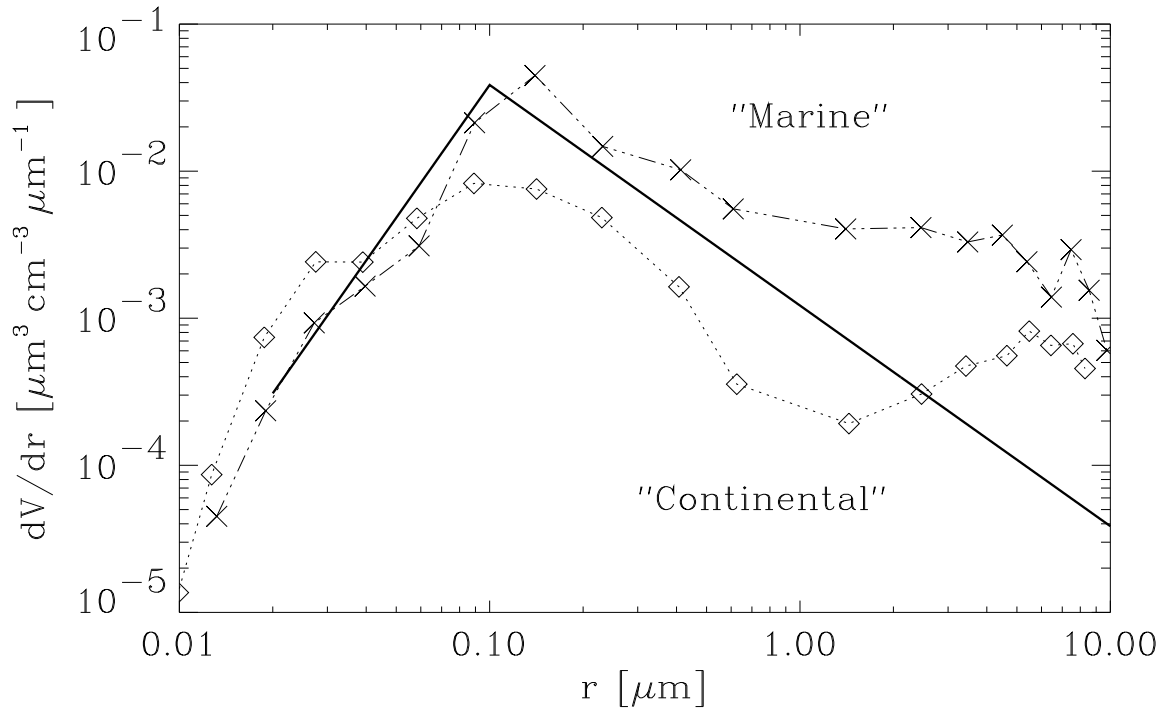


Figure 12.

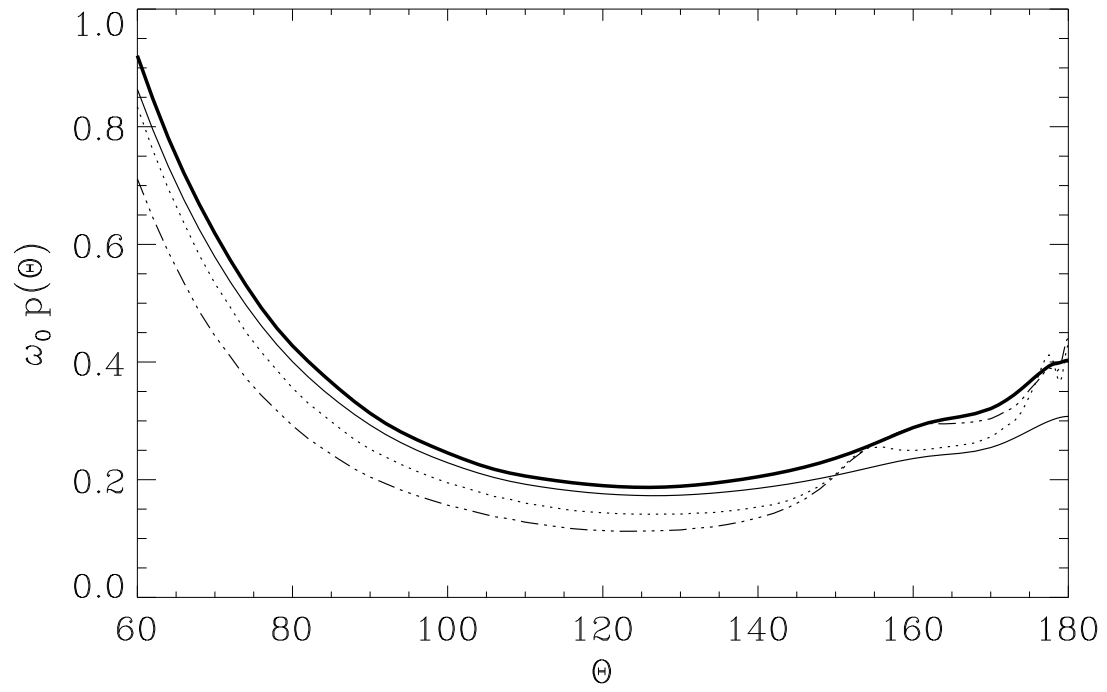


Figure 13.

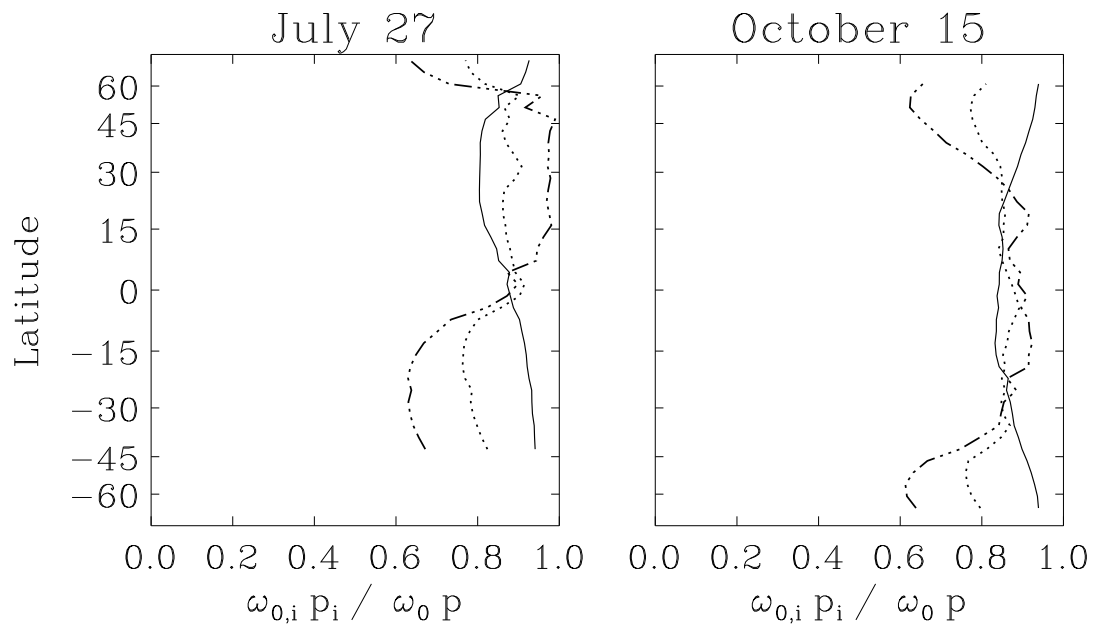


Figure 14.

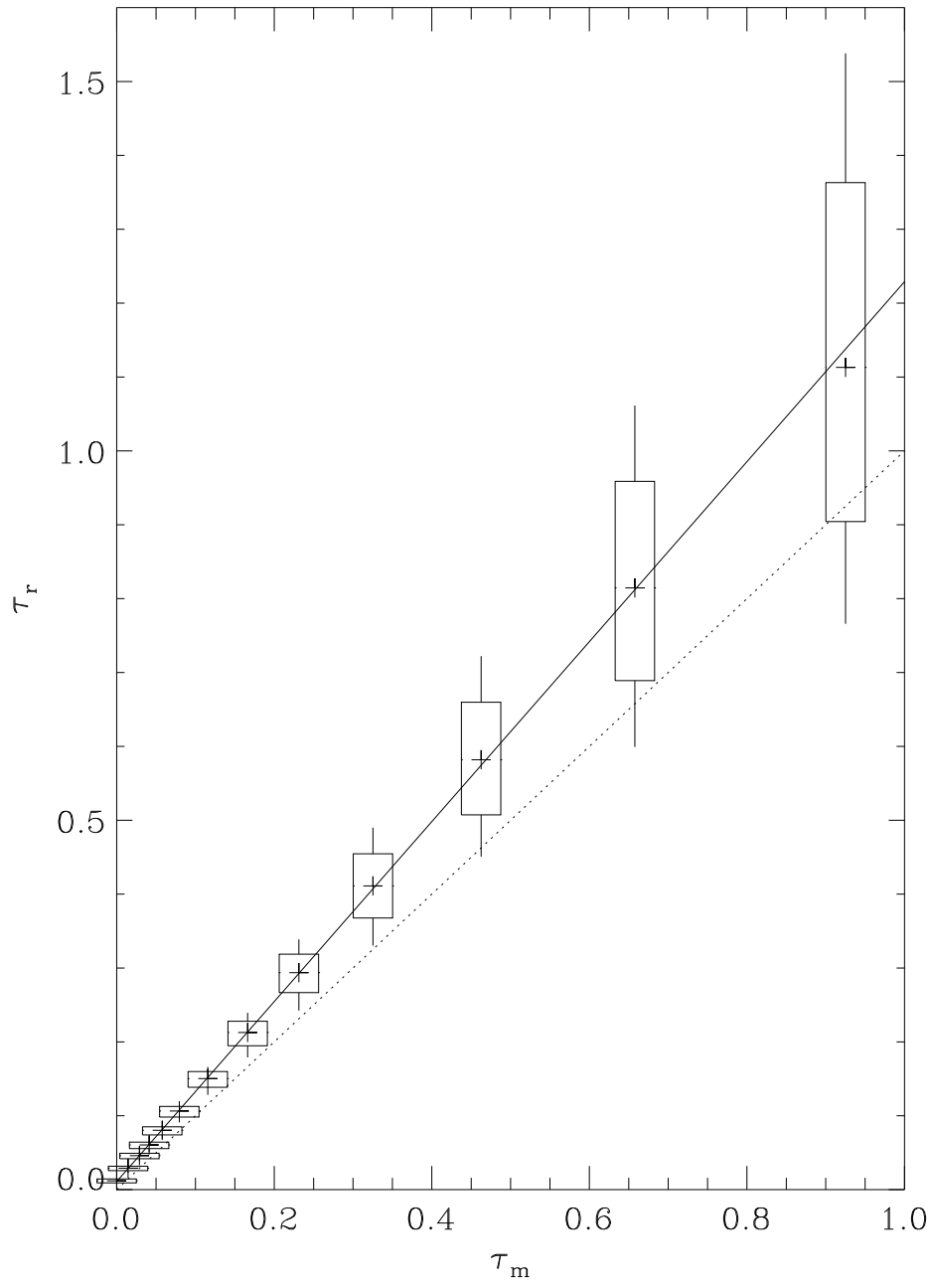


Figure 15.